Estimating snow accumulation and ablation with L-band InSAR

Jack Tarricone[1], Ryan W. Webb[3], Hans-Peter Marshall[4], Anne W. Nolin[2,1], and Franz J. Meyer[5]

[1]Graduate Program of Hydrologic Sciences, University of Nevada, Reno, Reno, NV, USA
[2]Department of Geography, University of Nevada, Reno, Reno, NV, USA
[3]Department of Civil & Environmental Engineering & Construction Management, University of Wyoming, Laramie, WY, USA
[4]Department of Geosciences, Boise State University, Boise, ID, USA
[5]Geophysical Institute, University of Alaska Fairbanks, Fairbanks, AK, USA

Correspondence: Jack Tarricone (jtarricone@nevada.unr.edu)

Abstract. Snow is a critical water resource for the western US and many regions across the globe. However, our ability to accurately measure and monitor changes in snow mass from satellite remote sensing, specifically its water equivalent, remains a challenge in mountain regions. To confront these challenges, NASA initiated the SnowEx program, a multi-year effort to address knowledge gaps in snow remote sensing. During SnowEx 2020, the UAVSAR team acquired an L-band Interferometric

5 Synthetic Aperture Radar (InSAR) data time series to evaluate the capabilities and limitations of repeat-pass L-band InSAR data for tracking changes in snow water equivalent (SWE). The goal was to develop a more comprehensive understanding of where and when L-band InSAR can provide snow mass change estimates, allowing the snow community to leverage the upcoming NASA-ISRO SAR (NISAR) mission. Our study analyzed three InSAR image pairs from the Jemez River Basin, NM, between 12-26 February 2020. We developed an end-to-end UAVSAR InSAR processing workflow for snow applications. This open-

10 source approach employs a novel data fusion method that merges optical snow covered area (SCA) information with InSAR data. Combining these two remote sensing datasets allows for atmospheric correction and delineation of snow covered pixels. For all InSAR pairs, we converted phase change values to SWE change estimates between the three data acquisition dates. We then evaluated InSAR-derived retrievals using a combination of optical snow cover data, snow pits, meteorological station data, in situ snow depth sensors, and ground-penetrating radar (GPR). The results of this study show that repeat-pass L-band

15 InSAR is effective for estimating both snow accumulation and ablation with the proper measurement timing, reference phase, and snowpack conditions.

1 Introduction

1.1 Significance and Motivation

In the western US (WUS), seasonal mountain snowmelt produces approximately 70% of the annual discharge (Li et al., 2017a), and is the primary water source for about 60 million people (Stewart et al., 2004). To adequately manage this resource, an accurate accounting of the spatiotemporal variations in snow water equivalent (SWE) is needed (Bales et al., 2006). Climate change is affecting the stationarity of the WUS hydrologic cycle (Milly et al., 2008), causing an overall decline in mountain snowpack (Mote et al., 2018), and emphasizing the importance of properly monitoring snow into the future (Siirila-Woodburn et al., 2021).

Water managers could benefit from regular repeat coverage of spatially distributed, low latency SWE data at spatial resolutions that are appropriate for mountain water forecasting. While remote sensing has made significant advances in measuring snow properties, there is still no remote sensing technique that can continually measure SWE from space for mountain hydrologic applications (Lettenmaier et al., 2015). Here, we explore L-band InSAR for monitoring changes in SWE.

1.2 Background and Previous Work

The most effective and widely used SWE estimation technique combines suborbital lidar (Deems et al., 2006; Trujillo et al., 2007) with hyperspectral imaging (Nolin et al., 1993) to produce both snow depth and fractional snow covered area (fSCA) at the watershed scale. To convert these measurements into SWE requires spatially distributed snowpack energy balance modeling (Painter et al., 2016). Like all optical techniques, lidar and hyperspectral imaging are limited by cloud cover, which can be frequent in mountain environments, and global spaceborne monitoring with lidar is not currently practical.

Since the 1970's, spaceborne passive microwave radiometers have used brightness temperature to estimate SWE at hemispherical scales (Rango et al., 1979). More recent studies utilized the Advanced Microwave Scanning Radiometer-EOS (ASMR-E) and the Scanning Multichannel Microwave Radiometer (SMMR) to continue the development of this SWE estimation technique (Derksen et al., 2002; Vuyovich et al., 2014). These instruments produce data on the spatial scale of tens of kilometers, limiting their ability to capture the topographic and snowpack heterogeneity of mountain environments. Passive microwave retrievals are also limited to dry snowpacks less than approximately 1 m of snow depth due to signal saturation (Foster et al., 2005).

While passive microwave remote sensing is not well suited for mountain environments, active microwave (radar) has shown promise for snowpack monitoring. Time-of-flight approaches have been used for decades from ground-based (Gubler and Hiller, 1984; Marshall and Koh, 2008) and airborne (McGrath et al., 2018; Lewis et al., 2017) platforms. Synthetic aperture radar (SAR) is an active microwave remote sensing technique that addresses the two main deficiencies in both optical and passive microwave; it can penetrate through clouds and has a spatial resolution on the scale of tens of meters instead of kilometers.

Spaceborne applications of SAR for estimating snow properties have mostly focused on backscatter approaches, where shorter wavelengths (Ku- and X-band) have been used to estimate SWE (Rott et al., 2010; Yueh et al., 2009; King et al.,

2018; Zhu et al., 2021). However, this method requires a complex dense media radiative transfer model (DMRT) with input parameters that not only include snow density (ρ_s) and snowpack liquid water content (LWC), but also parameters such as snow stratigraphy, snow grain size, and ground surface conditions. The snow microstructure parameters are challenging to precisely estimate over large spatial scales (Rutter et al., 2019).

55   SAR is proven for measuring snow wetness (Nagler and Rott, 2000; Nagler et al., 2016; Lund et al., 2020) as wet snow attenuates the radar signal, causing a decrease in backscatter intensity when compared to dry snow conditions. New backscatter methods are being developed to measure snow depth at C-band (Lievens et al., 2019, 2022). This technique shows promise especially in deeper snowpacks (>1 m), but the underlying physics governing the retrievals are not yet well characterized.

    Recently, the use of Interferometric Synthetic Aperture Radar (InSAR) to estimate SWE has become an area of interest
60 because of the higher temporal (12 days) frequency and L-band (~24 cm) wavelength of the future NASA-ISRO SAR (NISAR) mission (Rosen et al., 2017). InSAR uses the differences in radar phase between subsequent overpasses to estimate surface displacement. The InSAR SWE theory, initially proposed by Guneriussen et al. (2000), relates changes in the interferometric phase of a radar signal to changes mass of dry snow on the ground between acquisitions.

    A series of studies have shown further utility of these InSAR methods for snow such as Rott et al. (2003) in Austria, and
65 Deeb et al. (2011) on Alaska's north slope using European Remote-Sensing Satellite (ERS-1) C-band radar. Leinss et al. (2015) conducted an intensive season-long ground-based dual-frequency (Ku- and X-band) interferometric experiment in Finland with measurements every four hours, where they found the method was successful for continually measuring SWE in dry taiga snow, but that liquid water and vegetation quickly cause coherence loss at these higher frequencies.

    More recent studies have also used C-band radar from various space-borne platforms. The Sentinel-1 A/B radar was utilized
70 in Finland, leveraging the more consistent overpass repeat cycle (Conde et al., 2019). Li et al. (2017b) analyzed two InSAR pairs Envisat ASAR instrument in Tianshan Mountains of northwestern China, where they found promising results but were limited by large interferometric temporal baselines and the lack in situ validation data. Eppler et al. (2022) used a nine year RADARSAT-2 time series in Canada to develop "SlopeVar", a method for estimating SWE change without phase unwrapping by spatially correlating phase sensitivity to local topography. Nagler et al. (2022) conducted an airborne L- and C-band exper-
75 iment in the Austrian Alps in preparation for Radar Observation System for Europe in L-band (ROSE-L). While their results are preliminary, they show good performance for tracking snowfall events at L-band because of it's lack of impairment from 2π phase wrapping ambiguities.

    These orbital InSAR studies showed promise for estimating SWE but lacked sufficient temporal length and variety of vegetation, topography, and snowpack characteristics. Moreover, they also lacked adequate validation data and small spatial scale
80 to thoroughly understand the technique's limitations and synergies with other types of snow measurements.

1.3   Research Objectives

To address these InSAR-derived SWE limitations, the 2020 NASA SnowEx campaign (Brucker et al., 2019) conducted an Uninhabited Aerial Vehicle Synthetic Aperture Radar (UAVSAR) L-band InSAR time series flight campaign at 13 research sites across the WUS. The goal of the 2020 SnowEx experiment was to test L-band InSAR's ability to measure SWE changes

85 in a wide range of geographic locations, snow conditions, and land cover types with corresponding in situ ground-based observations. InSAR-derived snow depth changes measured over a two week interval on the open western end of Grand Mesa, CO in February 2020 showed high correlation ($r^2 = .76$) with snow depth differences measured by coincident repeat lidar from the same time period. RMSE differences between the two 5 m resolution depth change maps was within typical lidar error (<5 cm) (Marshall et al., 2021).

90 The overall goal of this study is to assess the performance of L-band InSAR for monitoring SWE changes in an environment where there is both snow accumulation and ablation. Currently this UAVSAR-based approach has only been applied to dry snow conditions, with accumulation and wind redistribution, but not melt. Towards this end the specific objectives of the work presented here are to (1) analyze InSAR SWE retrievals over a complex mountain region, and (2) validate the retrievals using satellite and in situ data.

2   Methods

To achieve our objectives we analyzed three interferometric image pairs that were acquired over the Jemez Mountains, New Mexico (Figure 2a). First, we developed a novel open-source processing work flow that (a) corrects the observed interferometric phase for atmospheric delay and (b) corrects incidence angle error effects by using improved incidence angle estimates derived from airborne lidar. We then computed spatial changes in SWE over the study area (Figure 2c), and evaluated our SWE 100 retrievals using optical fSCA, ultrasonic snow depth sensors, GPR, and in situ snow depth measurements.

2.1   InSAR for detecting SWE changes

InSAR is an active remote sensing technique that uses the differences in phase to map surface topography (single-pass) (Zebker and Goldstein, 1986) or measure changes to the Earth's surface (repeat-pass) (Goldstein and Zebker, 1987). Using the precise location of the orbit or flight pattern, the phase difference between the two (repeat-pass) acquisitions can calculate deformation 105 on the centimeter scale. Traditionally repeat-pass InSAR, where the sensor scans the same area at two different times, has been used to map tectonic and geomorphic activity on the Earth's surface, ice sheet velocity, and volcanic activity (Mouginot, 2012; Rosen et al., 2000).

For snow applications, Guneriussen et al. (2000) theorized a relationship between InSAR phase change and variation in dry snow water equivalent (SWE) between acquisitions. Dry snow has a low attenuation rate of the radar signal, and at frequencies 110 below 10 GHz (Marshall et al., 2005; Ulaby et al., 1984) the majority of the backscatter stems from the snow ground interface. Dry snow and the atmosphere have different dielectric properties, causing a refraction or directional change of the radar propagation path, and a decrease in speed when the signal propagates through the snow layer (Figure 1). The refraction and wave speed are controlled by the refractive index of snow, which is governed by ρ_s. We leverage these previous studies to develop a current workflow applied to UAVSAR data acquisitions.

115 To isolate the SWE change impacts on the phase, other factors impacting phase must be identified and compensated for. Outlined in Deeb et al. (2011), total interferometric phase includes the following contributions:

$$\phi_{total} = \phi_{flat} + \phi_{topo} + \phi_{atm} + \phi_{snow} + \phi_{noise} \tag{1}$$

where ϕ_{flat} and ϕ_{topo} are phase impacts from flat Earth and local topography, which are both already accounted for in the UAVSAR InSAR processing chain using the Shuttle Radar Topography Mission (SRTM) DEM as input. For UAVSAR, ϕ_{noise}

120 is mainly associated with uncertainty with the plane's GPS and slight variations in path between the two acquisitions. These errors are also accounted for within the UAVSAR processing workflow. Hence, for UAVSAR data, extracting ϕ_{snow} from the observed phase ϕ_{total} mostly requires an accurate compensation of ϕ_{atm}, which is the phase influence from the atmosphere. Refer to Section 2.4 for a detailed explanation of how ϕ_{atm} is addressed in our approach.

Once ϕ_{snow} is isolated, the measured phase shifts are used to estimate SWE using the following equation proposed by

125 Guneriussen et al. (2000), which accounts for both the path length change caused by refraction, and the change in wave speed in snow:

$$\Delta\text{SWE} = -\frac{\Delta\phi_{snow}\lambda}{4\pi} \cdot \rho_s \cdot \frac{1}{\cos\theta - \sqrt{\epsilon_s - \sin^2\theta}} \tag{2}$$

where ΔSWE is change in SWE between acquisitions, λ is the radar wavelength (23.84 cm for UAVSAR), θ is the radar incidence angle, and ϵ_s is the real part of the dielectric permittivity of snow. For dry snow, there is a direct relationship between

130 ϵ_s and ρ_s.

2.2 Description of the Study Area

Located in northern New Mexico, U.S.A., the Jemez Mountains and Jemez River are on the southern extent of the Rocky Mountains (Figure 2a). The extent of the UAVSAR swath encompasses portions of Valles Caldera National Preserve (VCNP) (35°53'N, 106°32'W) (Figure 2b). This area is mainly a mountain conifer forest environment consisting of Douglas fir, white

135 fur, and blue spruce. VCNP is surrounded by lower elevation semi-arid desert. Within the swath also lies the Valles Caldera, a 25-km wide volcanic structure dating back about 1.2 million years. Within Valles Caldera, Valle Grande (VG) (Figure 2c) is an extensive open grassland where field measurements took place for this study. Many resurgent lava domes form peaks over the grassy valleys, the highest of which is Redondo Peak (3430 m a.s.l.). About 50% of the total precipitation falls in the summer months as rain from convective monsoonal storms, and the rest falls in the winter as snow. The water in this area drains into

140 the East Fork of the Jemez River and eventually to the the Rio Grande. The nearby Quemazon Natural Resource Conservation Services (NRCS) Snow Telemetry (SNOTEL) site (35°55'N, 106°24'W, 2898 m a.s.l.) has a 1980-2022 average peak SWE of 22.4 cm.
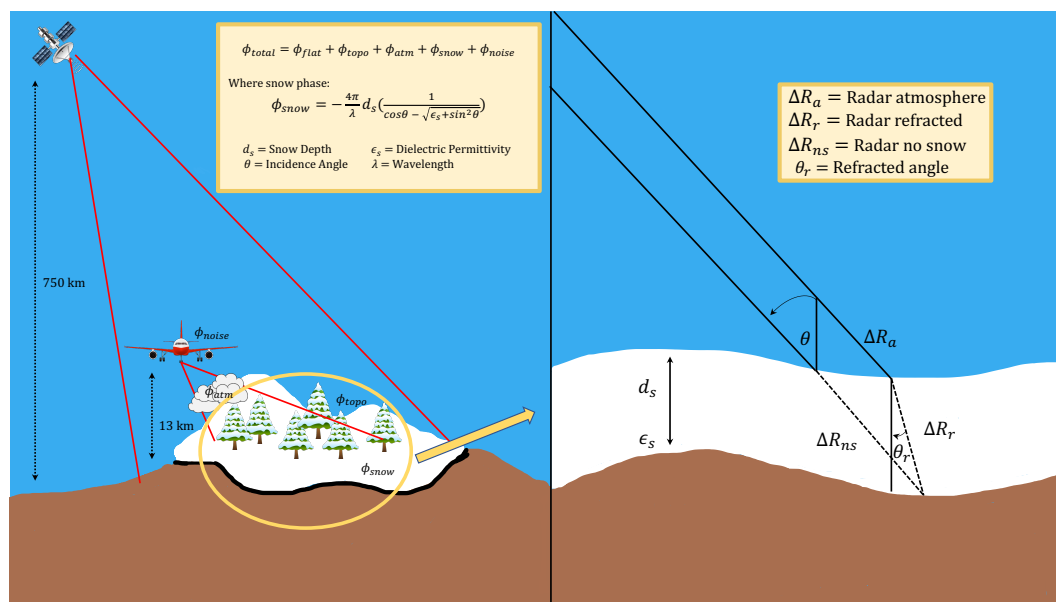
Figure 1. (Left) Graphic showing the factors affecting radar ϕ_{total} for airborne and orbital SAR. (Right) Diagram of how radar wave propagates with no snow (ΔR_{ns}), and with snow ($\Delta R_a + \Delta R_r$), at a certain radar incidence angle (θ). The amount of refraction (θ_r) and change in wave speed are controlled by the snow dielectric permittivity (ϵ_s), which is a function of snow density (ρ_s).

2.3 Data Description

2.3.1 Remote Sensing data

145 UAVSAR is a fully polarimetric L-band radar deployed on a NASA Gulf Stream III aircraft, traditionally flown at ~13,700 m with a 16 km nominal swath width (Hensley et al., 2008; Rosen et al., 2006). Detailed technical specifications of the radar are provided in Table 1.

UAVSAR data was accessed using the Python package uavsar_pytools (Keskinen and Tarricone, 2022). It utilizes asf_search API (https://github.com/asfadmin/Discovery-asf_search) for easier downloading, formatting, and analysis of UAVSAR data.

150 The flights used in this study occurred in the mornings of 12, 19, and 26 February 2020 (Table 2). The 12-19 and 19-26 February InSAR pairs were processed by the UAVSAR team at the NASA Jet Propulsion Laboratory (JPL), where they were unwrapped using the Integrated Correlation and Unwrapping (ICU) algorithm (Goldstein et al., 1988). The 12-26 February pair was processed locally from a Single Look Complex (SLC) stack using the Interferometric synthetic aperture radar Scientific Computing Environment (ISCE2) and unwrapped with the Statistical-Cost, Network-Flow Algorithm for Phase Unwrapping

155 (SNAPHU) algorithm (Chen and Zebker, 2001).

Landsat 8 fSCA (U.S. Geological Survey and Center, 2018) data was acquired for 18 February and 5 March 2020 (Figure 3). This data is generated using a spectral unmixing analysis based Snow Covered Area and Grain size (SCAG) algorithm
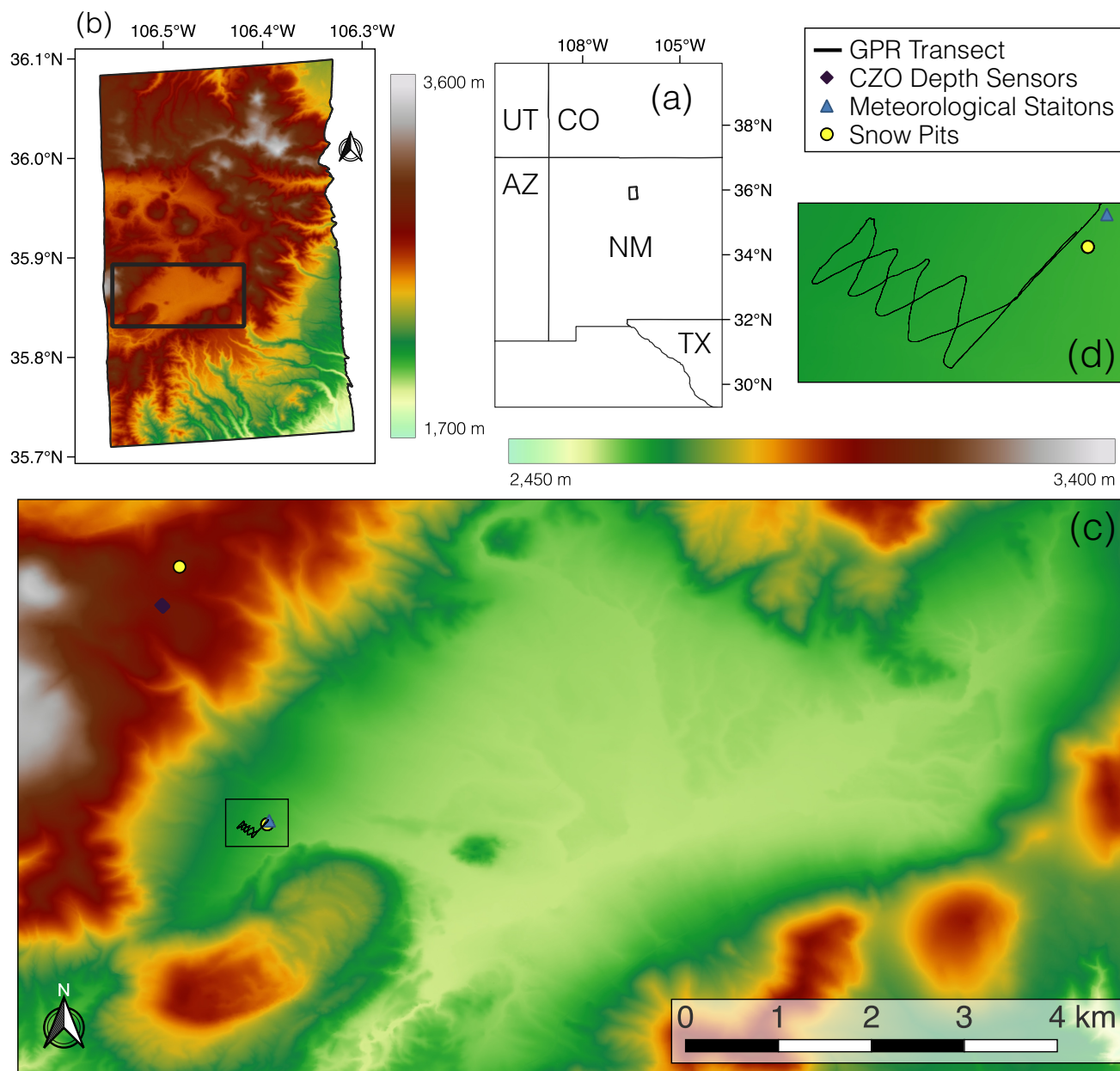
Figure 2. (a) Map showing the area of the UAVSAR acquisition (black outline) in the Jemez Mountains, NM. (b) DEM of the UAVSAR acquisition provided by NASA, with a black rectangle outlining VG and the surrounding hill slopes. (c) Lidar DEM of VG with the two snow pit locations shown by yellow circles, HQ meteorologic station by a blue triangle, six CZO snow depth sensors by black diamonds, and the GPR transect shown as a black line. (d) A close up of the GPR transect with the HQ Met snow pit and meteorologic station displayed.
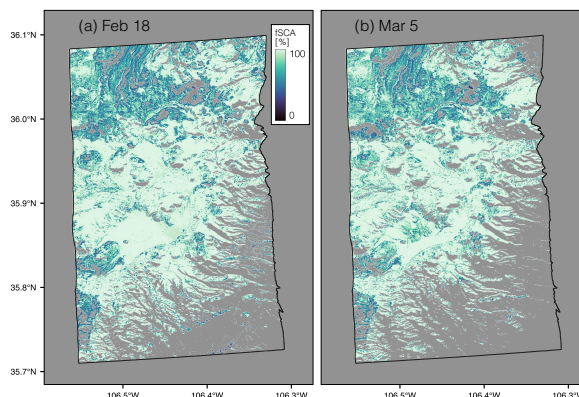
Figure 3. Landsat derived fSCA in the UAVSAR swath extent from (a) 18 February 2020 (b) 5 March 2020. Snow melt between these two days caused both a reduction in scene wide SCA and fSCA within the VG meadow.

Table 1. Technical Specifications of the UAVSAR L-band radar.

Parameter	Value
Wavelength	23.84 [cm]
Frequency	1.26 [GHz]
Polarization	Quad Pol
Bandwidth	800 [MHz]
Pulse Length	40 [μs]
Radar Look Direction	Left
Range Swath Width	16 [km]
Ground Range Pixel Spacing	6 [m]
Azimuth Spacing	7.2 [m]
Slant Range Spacing	4.99 [m]
Average Near Range Look Angle	28.01°
Average Far Range Look Angle	68.9°

developed for MODIS (Painter et al., 2009). The data processing workflow includes water-masking, cloud-masking, and canopy cover corrections (Selkowitz et al., 2017).

160 **2.3.2 Snow Pit and Meteorologic Station Data**

Snowpack information was collected at two pit locations during each of the three UAVSAR overflights (Marshall et al., 2022). The Headquarters Meteorologic station (HQ) pit was located at 35°51'30"N, 106°31'17"W, at an elevation 2650 m. The Burned Area (BA) pit was located near Redondo peak at 35°53'18"N, 106°31'57"W, at an elevation of 3045 m (Figure 2c).

Measurements of snow depth, stratigraphy, ρ_s, ϵ_s, temperature, and grain size were recorded for each pit. ϵ_s was measured
165   using an A2 Photonics WISe instrument (A2P, 2021). Summary statistics from each pit are located in Table 2. Interval boards,
which are small plastic manual precipitation gauges placed on the snow surface used to track new snow accumulation, were
located in close proximity to each of the two snow pits.

The Western Climate Research Center (WRCC) deployed two meteorologic stations that measured snow depth, air temper-
ature, wind speed, wind direction, and incoming solar radiation. The first station is the aforementioned HQ station, and the
170   second is located on Redondo Peak near the BA pit (35°53'02"N, 106°33'13"). Six ultrasonic snow depth sensors originally
installed by Molotch et al. (2009) and utilized in subsequent studies by (Musselman et al., 2008; Harpold et al., 2015), were
used to measure variations in snow depth near the BA pit (Figure 2c).

Table 2. Snow pit data collected for the UAVSAR time series. Data was collected on 20 February and not during the 19 February flight date.
No BA pit was dug on February 12. Bulk ρ_s is reported, and no ϵ_s was collected at the BA pit.

Pit	Date	UAVSAR start	Pit start	Depth [cm]	ρ_s [kg m^{-3}]	SWE [cm]	Mean ϵ_s	Condition
HQ	2/12	0946 MT	1305 MT	78	261	20.3	1.26	Mostly Dry
HQ	2/20	1010 MT	1156 MT	67	302	20.2	1.39	Melting
HQ	2/26	1027 MT	1157 MT	66	309	20.4	1.29	Melting
HQ	3/04	1105 MT	NA	57	342	19.5	1.56	Melting
BA	2/12	0946 MT	NA	NA	NA	NA	NA	NA
BA	2/20	1010 MT	1224 MT	80	290	23.2	NA	Dry
BA	2/26	1027 MT	1139 MT	82	290	23.8	NA	Dry
BA	3/04	1116 MT	NA	76	307	23.3	NA	Dry

2.3.3 GPR Survey

We used Ground Penetrating Radar (GPR) to obtain distributed SWE estimates along a transect for ground validation purposes
175   (Marshall et al., 2005; Webb, 2020). A GPR pulse is an electromagnetic wave that travels through the snowpack and is reflected
off changes in material properties such as ρ_s, with the strongest reflection often from the snow-soil interface at L-band (Brad-
ford et al., 2009; Holbrook et al., 2016; Webb, 2017). For this study, two-way-traveltime (t_2) of GPR waves through snow were
obtained along transects. We used a Mala Geoscience, Inc. ProEx control unit pulse GPR system with an 800 MHz shielded
antenna. The antenna was fixed in place on a plastic sled towed behind the operator. A GPS antenna connected to the ProEx
180   control unit registered location information every second.

Radar pulses were triggered on 0.05 s intervals using eight times stacking. The average survey travel speed was ~0.5 m s^{-1}
resulting in ~40 returns per meter. The ReflexW 2D Software package (Sandmeier and Straße, 2022) was used for time-zero
adjustment, taken as the first break in the first wavelet and a dewow filter and spherical divergence correction to compensate

for signal attenuation. The dewow filter removes low frequency content by calculating a running mean that is subtracted from a

185 central point. The reflection of the snow–soil interface was then selected at the first break prior to the first peak of the reflection. Topographic correction was performed by dividing t_2 by the cosine of the ground surface slope at that location.

The ϵ_s of snow is sensitive to ρ_s and LWC (Bradford et al., 2009; Heilig et al., 2015; Webb et al., 2018), and is related to the velocity (v) of the radar wave through snow:

$$v = \frac{s}{\sqrt{\epsilon_s}} \tag{3}$$

190 where s is the speed of light in a vacuum (~0.3 m ns^{-1}). For this study, the ϵ_s was directly observed in snow pit observations using an A2 Photonics WISe instrument. The observed ϵ_s was then used to estimate a velocity to distribute snow depth estimates along GPR transects.

$$d_s = \frac{vt_2}{2} \tag{4}$$

These depth estimates were then converted to SWE by multiplying snow depth by the pit-observed bulk ρ_s for direct com-

195 parison to UAVSAR derived ΔSWE (described further in Section 2.6). When using this approach of GPR observations in combination with a pit-observed bulk ρ_s, we can expect to observe SWE values within 5% at the frequency used (Marshall et al., 2005). We calibrated our GPR ΔSWE data to the observed ΔSWE at the snow pit. To do this, we defined a bias as the observed mean ΔSWE difference between all GPR observations within 20 m of the snow pit and the SWE measured at the pit. We then removed this bias from the entire GPR dataset to create a directly comparable dataset relative to the UAVSAR derived

200 ΔSWE. This is a similar method as described below to tether the UAVSAR data to snow pit observations.

2.4 InSAR Atmospheric Correction

Radar signals can penetrate a moist and cloudy atmosphere, but the variation in dielectric properties between wet and dry air can significantly affect the radar signal (Ferretti et al., 2001). While substantial research has been conducted for correcting both tropospheric and ionospheric effects from satellite-based SAR (Meyer, 2011; Yu et al., 2018), suborbital SAR is both less

205 common and has different correction considerations due to the lower acquisition altitude and often shallower and more diverse observation geometries. However in one recent study, Michaelides et al. (2021) laid out an approach to successfully corrected UAVSAR atmospheric delay using a high-pass and low-pass filtering sequence.

Tropospheric atmospheric delay effects can be divided into two parts, the dry delay and the wet delay. The dry delay is caused by variations in temperature and pressure and is often considered less significant than the wet delay for spaceborne

210 sensing (Zebker et al., 1997). Wet delay is caused by spatial (within swath) and temporal (between acquisitions) variations in atmospheric water vapor concentrations (Danklmayer et al., 2009).

As seen in Figure 4a, the raw unwrapped phase data shows a noticeable near-to-far range phase ramp. For this UAVSAR flight, the average altitude was 12.9 km, compared to a satellite that traditionally orbits around 750 km. This vastly lower
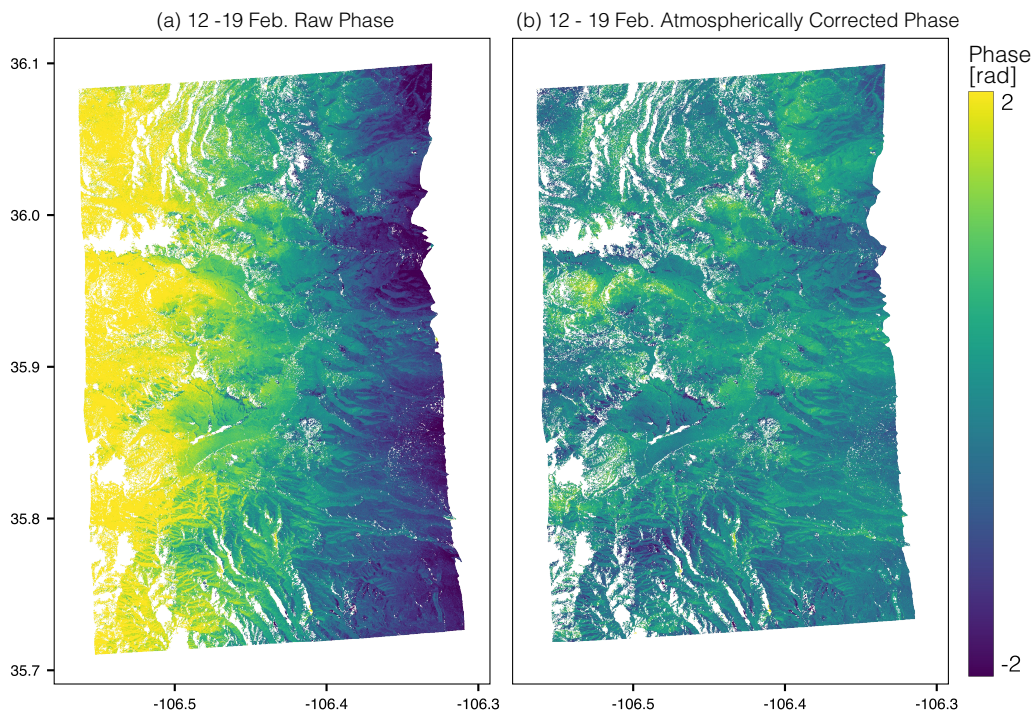
Figure 4. (a) Shows the uncorrected unwrapped phase from the 12-19 February pair. There is a linear ramp in the phase that is increasing from near-to-far range (east to west) which is a distance of approximately 22 km. (b) Shows the atmospherically corrected phase change data.

sensing altitude causes a larger diversity of look angles and radar path length variations between the near and far ranges of the radar swath to emerge. The radar path length vector (PLV), or the distance between a point on the ground and the radar, ranged between 11.4 km and 27.8 km. The look angle varied from 28.51° in the near range to 69.01° in the far range. Thus, the radar wave in the far range is traveling through more atmosphere than the near range by a factor of 2.4.

Assuming a spatially homogeneous change in atmosphere between acquisitions, we developed a method to correct for the phase ramp by calculating the distance from the radar to a point on the ground for every pixel in the scene, also known as the path length vector (PLV). The PLV is mostly dependent on the near to far range position in the scene, but also varies with local topography. PLV is calculated by geocoding the easting (e), northing (n), and up (u) components of the SLC data. The distance is then calculated by:

$$PLV = \sqrt{e^2 + n^2 + u^2} \tag{5}$$

Embedded within the atmospheric delay phase signal is the smaller scale snowpack variation phase signal. By only calculating the atmospheric delay of snow free pixels from the Landsat fSCA product on 18 February, we were able to confirm the bulk
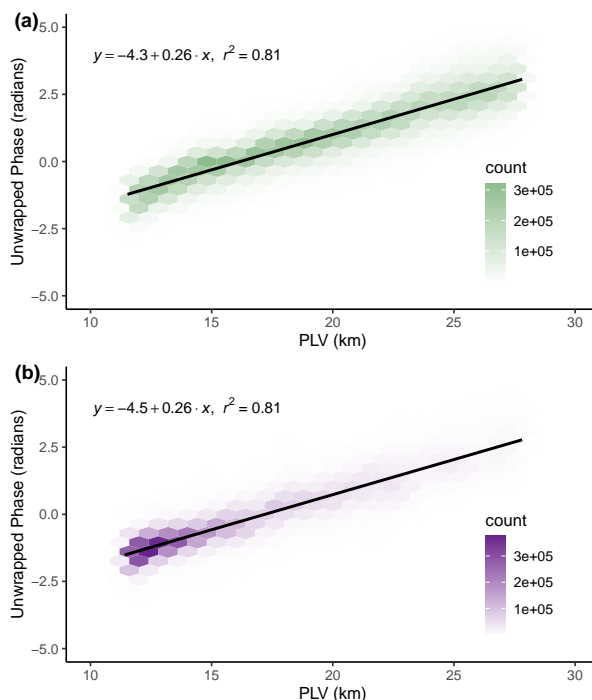
Figure 5. Density scatter plots showing the relationship between unwrapped phase and the radar PLV for the 12-19 February InSAR pair for (a) snow covered pixels and (b) snow free pixels. The similarity in the two plots shows the large scale phase signal is atmospheric and not snowpack related.

of the observed signal is atmospheric and not snowpack-related (Figure 5b). Using data from meteorological stations, we know there was not a large scale snowfall event between the two flights. Using the linear relationship (r^2 = .81) between PLV and phase shown in Figure 5a, we subtract the estimated atmospheric component from the raw data to achieve the atmospherically corrected image (Figure 4b). This correction was also applied to 12-26 February pair as it showed the same atmospheric delay.

230 ## 2.5 Generating Local Incidence Angle Data

The local incidence angel (θ) angle is the angle between the ground surface normal and the radar line of sight calculated on a per-pixel basis (Figure 1). The angle is calculated by deriving the surface normal from a DEM and computing the dot product with radar path length vector:

$$\theta = cos^{-1}(-\hat{n} \cdot PLV) \tag{6}$$

235 Where θ is the local incidence angle, $\hat{n}$ is the surface normal, and PLV is the radar line of site vector length. θ varies with respect to local topography and the PLV. θ affects the distance the radar wave will travel through the snowpack and is a direct
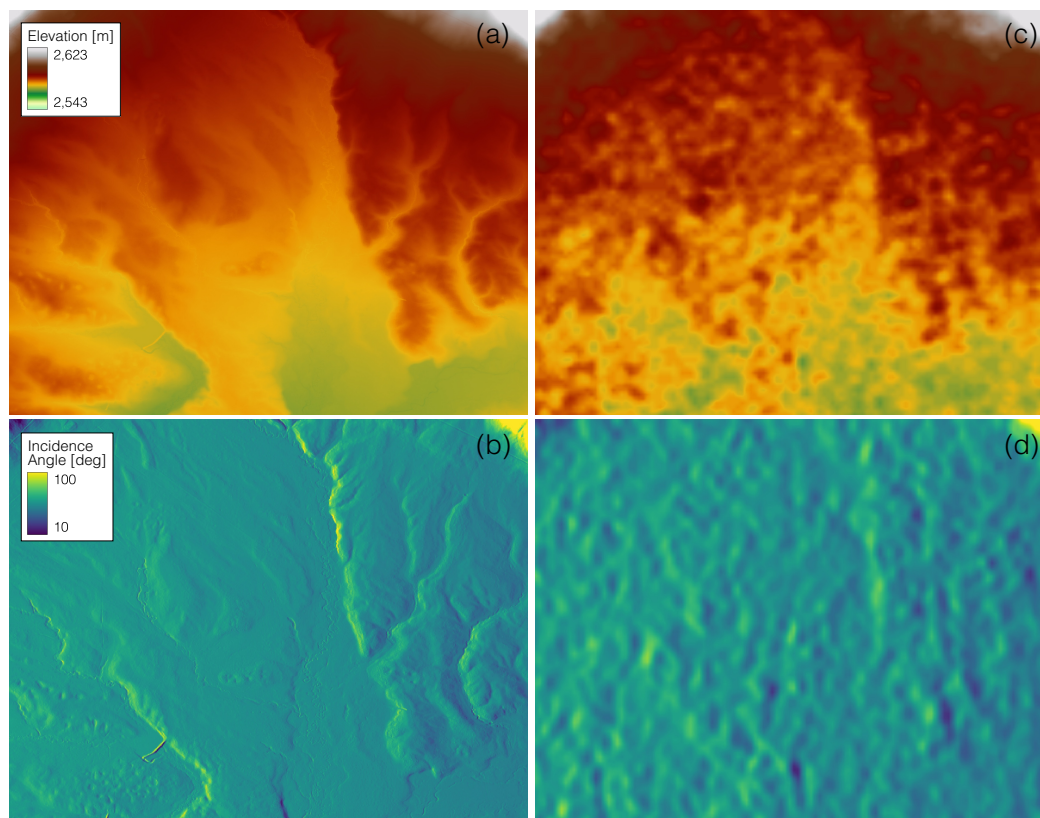
Figure 6. The snow free ground surface and UAVSAR θ in a portion of the VG meadow for (a) the lidar DEM (b) the new θ data generated from the lidar DEM (c) the JPL SRTM DEM (d) the θ data provided by JPL. Gullies and small stream channels are easily discerned from the lidar data, while the SRTM DEM shows large undulating mounds.

input into the SWE change inversion algorithm (Equation 2). We found significant errors within the original SRTM DEM used in UAVSAR data processing (Figure 6c). The meadow in Valle Grande is relatively flat and smooth outside of river channels and gullies. However, the original DEM shows mounds and undulations on the order of 10 to 20 m throughout the meadow

240   that do not accurately represent the ground surface. These DEM errors propagate into the estimate of θ (Figure 6d), which is then input into the SWE change equation, causing errors in SWE change estimations.

The original DEM used in interferometric processing is an SRTM 30 m product that had been downsampled to the native UAVSAR resolution of 6 m. The Spaceborne Imaging Radar-C/X-band Synthetic Aperture Radar (SIR-C/X-SAR) acquired the single-pass interferometric from the Space Shuttle Endeavor in February 2000. During the midwinter acquisition period, snow

245   cover was present at our study site. Radar waves a C-band can penetrate dry snow up to several meters, but the presence of liquid water changes the dielectric and scattering properties of the snowpack (Farr et al., 2007), influencing penetration depth, and likely caused the observed issues with the initial DEM.

We generated new θ data using a snow free lidar DEM (Figure 6a) acquired in 2010 for the Catalina-Jemez Critical Zone Observatory (CZO) (OpenTopography, 2012). The high spatial resolution (1 m) and lack of interference from snow provide a

250   more reliable starting point to calculate θ. By using the PLV and the lidar DEM, the new θ data better represent the bare ground surface of VG (Figure 6b).

2.6   Calculating SWE Change

To begin the SWE change estimation, the three InSAR pairs were masked with Landsat fSCA data collected on 18 February 2020. All pixels with >15% snow cover were included to not mistakenly exclude pixels in the forest where the snowpack is

255   partially obstructed by forest canopy. Using Equation 2, ΔSWE values were calculated on a pixel-wise basis with inputs of λ_i (23.84 cm), ρ_s, ϵ_s, and the lidar derived θ. ρ_s and ϵ_s are averages of the two snow pit values (Table 2) between the two acquisition dates.

InSAR phase differences produce a relative measurement of SWE, therefore this data need to be tethered to a point on the ground to estimate absolute change. Since there was near zero SWE change at the HQ snow pit between the three UAVSAR

260   acquisitions (Table 2), we used this location as our InSAR known change point. This SWE change of -.1 cm for 12-19 February and .2 cm for 19-26 February is well within the margin of measurement error (10%) for the snow pit observations. To account for error within both GPS snow pit location and the geocoding of the InSAR data, the ΔSWE values for the eight surrounding pixels were averaged and this value was subtracted. To calculate the cumulative ΔSWE, the 12-19 February and 19-26 February were masked so only pixels that occurred in both scenes were considered, and then added together.

265 ## 3   Results

3.1   InSAR Polarization, Unwrapped Phase, and Coherence

Three interferometric products - coherence, unwrapped phase, and the interferogram are produced for every InSAR pair. Coherence measures the consistency of the scattering characteristics within a pixel between InSAR acquisitions. Unwrapped phase is the estimated absolute phase change in a pixel, generated from the initially ambiguous interferogram, which is defined

270   modulo 2π.

When there is a significant change in the landscape scattering properties between InSAR acquisitions, phase noise and fringe discontinuities increase, coherence decreases, and the unwrapping algorithm performs less reliably (Balzter, 2001). We analyzed the coherence and unwrapped phase products for all four polarizations to assess their quality before implementing the SWE change equation. We found co-polarizations (HH & VV) to have the highest average coherence and the greatest

275   percentage of pixels preserved in the unwrapping process (Table 3) compared to cross-polarizations (VH & HV). We choose to analyze HH and only processed this polarization for the 12-26 February pair with ISCE2.

The right side of Figure 7 shows the coherence values in VG for the (a) 12-19 February, (b) 19-26 February, and (c) 12-26 February. In the coherence maps there are clear patterns with respect to topography and probable variations in snowpack

Table 3. UAVSAR unwrapped phase (UNW) and coherence statistics for the full scene (FS) and Valle Grande (VG). UNW Loss [%] is the percentage of pixels lost in the unwrapping process.

Pair	Polarization	FS Mean Coherence	VG Mean Coherence	FS UNW Loss [%]	VG UNW Loss [%]
12-19 Feb.	HH	.53	.50	9.4	7.7
12-19 Feb.	HV	.44	.34	17.7	42.0
12-19 Feb.	VH	.44	.36	23.7	56.9
12-19 Feb.	VV	.54	.50	8.9	12.8
19-26 Feb.	HH	.55	.52	5.0	4.1
19-26 Feb.	HV	.49	.38	8.2	10.7
19-26 Feb.	VH	.47	.37	11.8	17.4
19-26 Feb.	VV	.57	.54	4.3	3.7

LWC. The area of lowest coherence surrounds the main channel of the Jemez River (red dotted line) that flows through the south-central portion of VG. As seen in Figure 7d there is a variable area of low backscatter in all three amplitude images. This backscatter decrease is likely caused by snowpack LWC attenuating the radar signal. The spatial variability in LWC between acquisitions causes low coherence and the loss of pixels in the unwrapping processes for all three pairs in this riparian area. There are also horizontal streaks of low coherence and high backscatter within the images, likely a result of artifacts from the InSAR and SAR processing. These lines do not propagate into the unwrapped phase data and therefore are not of significant concern.

The left side of Figures 7a, 7b, & 7c show the unwrapped phase values for InSAR pairs. In the open meadow (blue dotted line), the unwrapping algorithm performs well, and most pixels are persevered except in the riparian area for the reasons described previously. The other primary source of low coherence and corresponding unwrapping pixel loss occurs on the forested hill slopes surrounding the VG meadow. Overall, the unwrapped data provides a high quality input into the SWE change inversion equation.

3.2 Mapping Changes in SWE

Figure 8 shows the ΔSWE results for 12-19 February, 19-26 February, 12-26 February, and the cumulative change between 12-26 February in VG. In Figure 8a (12-19 February), SWE has a mean change of -.52 cm, with much of the VG meadow showing similar change. The 99th and 1st percentile of the ΔSWE data are reported in Table 4. In the meadow the largest SWE losses occur on the south aspect slopes around gullies and terrain depressions. The northeast corner of the study area shows a consistent increase in SWE, on the order of less than a centimeter. While there are more pixels lost on the forested hill slopes, there is a pattern of more SWE loss on the south facing slopes than the north facing, which would make sense for melt impacts at this time of year.

Table 4. ΔSWE summary statistics from Figure 8 in [cm] for the four InSAR pairs analyzed. 12-26 February cumulative (CM) is created by adding the SWE changes from 12-19 February and 19-26 February pairs.

InSAR Pair	ΔSWE Mean	ΔSWE 99th%	ΔSWE 1st%	ΔSWE SD
12-19 Feb.	-0.52	2.34	-3.63	1.11
19-26 Feb.	-1.24	1.61	-4.80	1.30
12-26 Feb.	-2.67	2.07	-8.79	2.02
12-26 Feb. CM	-1.76	1.51	-6.80	1.62

Figure 8b (19-26 February), displays similar spatial patterns to the first pair. Overall the mean SWE loss was -1.24 cm for this time frame, with the same gully areas showing the greatest loss. The highest elevation occurs in the northwest corner of the scene near Redondo Peak, and it is the only place to show consistent SWE increases. These increases compared well with in situ snow depth sensors in the area (see Section 3.4). The pattern between SWE loss on south aspect slopes and a constant to slight gain of SWE on north aspect remains from the first pair, with the small storm explaining north aspect increases.

Figure 8c (12-26 February) is the only pair not processed by the UAVSAR team. It had a mean ΔSWE of -2.67 cm. The cumulative ΔSWE (Figure 8d) map was created by adding the values of Figure 8a and 8c together. The mean value of the cumulative SWE change was -1.76 cm, with a range of 1.51 to -6.8 cm. The patterns observed in the individual InSAR pairs become more evident in the both Figure 8c & 8d, with the greatest losses (3-6 cm) occurring in the gullies of the VG meadow and the south facing forested hill slopes above. Figure 9a compares the distribution of SWE change values for the 12-19 and 19-26 February pairs, and Figure 9b for 12-26 and cumulative 12-26 February pairs. 19-26 February shows more SWE loss than 12-19 February.

3.3 Changes in SWE: InSAR vs. GPR

We compared the ΔSWE InSAR results to GPR data collected between 12-26 February. The point GPR returns were rasterized to the 6 m UAVSAR resolution where only pixels with 30 or more GPR point observations were retained (n = 129). Figure 10 is a scatter plot of the 12-26 February and 12-26 February cumulative change (12-19 + 19-26 February) InSAR pairs compared with the GPR ΔSWE returns from the same time period. While no significant relationship was found, there is a relatively small difference in average ΔSWE from the two methods. It can be seen that the GPR observations center near a ΔSWE value of zero (mean of -0.17 cm) and the InSAR-derived ΔSWE shows slightly more negative values with a mean value of -2.34 cm.

Both of these methods were calibrated using the previously mentioned HQ snow pit and thus, this comparison shows a slight negative bias (loss of SWE) on the order of ~2 cm for the InSAR method for the conditions of this study. However, this likely represents a maximum error due to the five percent uncertainty of the GPR method, or ~1 cm SWE for each observation date, and therefore 1-2 cm for the GPR ΔSWE product. Additionally, the difference in timing between the UAVSAR overflight and the GPR survey of about three hours could have resulted in an increase of LWC in the snowpack during the GPR survey, and

therefore an underestimate of SWE loss, although this is likely minimal due to the re-freezing of the snow surface overnight and observed HQ pit temperatures. Thus, the observed InSAR ΔSWE difference of ~2cm relative to GPR observations provides an estimate of InSAR Δ SWE retrievals.

3.4 Comparison to In Situ Snow Depth Sensors

We compared seven in situ snow depth sensors to InSAR-derived SWE changes. Figure 11 is a time series of snow depths from seven ultrasonic sensors from 12-26 February. Six of sensors are located on Redondo Peak and one is on the HQ Met station in VG. The grey shaded area on the plot shows a small snowfall event starting the night of 22 February and ending 23 February. This snowfall is only registered in the higher elevation sensors and not in the HQ Met location. We see this same pattern for InSAR-based returns in Figure 8b (19-26 February). VG shows mostly SWE loss, while the higher elevation area in the northwest corner of the plot shows an area of increase, which is captured by the in situ sensors.

In situ snow depths were converted to SWE by multiplying by the bulk ρ_s of 290 kg m^{-3} (from snow pit observations) for the three pairs when there was no measurable snowfall. We used new ρ_s of 240 kg m^{-3} measured from the BA pit interval board for the 19-26 February pair. These SWE measurements were compared against the InSAR pixel's they're located in Figure 12 (n = 28, r^2 = .3).

3.5 ΔfSCA vs. InSAR ΔSWE

We compared the InSAR ΔSWE from 12-26 February (Figure 13a) to ΔfSCA between 18 February and 5 March (Figure 13b). The InSAR data was aggregated up to the 30 m Landsat resolution. While these datasets measure two different variables (SWE vs. fSCA) during different acquisition periods, the comparison of snow ablation patterns provides useful information when attempting to validate the experimental InSAR results.

Several landscape features are prevalent in both datasets. The long gully that runs from the north central area of VG to the Jemez River is shown clearly in both maps. Other smaller gully's are also clearly visible. There are both SWE and fSCA losses on the the south facing hillslopes surrounding the VG. Both of these patterns are being driven by these areas receiving more direct solar radiation. In the northwest corner of the image the InSAR-derived map shows a small area of SWE increase and the fSCA image shows no loss in this area.

Limited fSCA loss occurred in much of VG meadow, while 1-3 cm losses in SWE were recorded throughout the whole meadow. For optical images to show fSCA loss, bare ground must appear in the pixel. For the majority of snow melt season, pixels lose SWE while still being completely snow covered. The fSCA product also shows more areas of melt than the ΔSWE product, which can be explained by the eight day difference in date of the last acquisition (26 February vs. 5 March). During that eight day period the field teams noted that melt started to progress at a higher rate which, and areas of the meadow became bare seen in both the fSCA imagery and by field teams. fSCA gains are recorded in the forested areas south of VG. This uncertainty arises from how the algorithm deals with sub-canopy forest snow estimation.

4 Discussion

4.1 Key Findings

During the study time frame, there was one localized measurable precipitation event on Redondo Peak and temperatures were diurnally fluctuating below and above freezing during the study period (Figure 14). With the snowpack going through daily partial freeze-thaw cycles, creating large sintered grains, and average wind speeds of 2.4 m s^{-1}, there is a low probability of blowing snow being a significant driver of SWE loss. This is further confirmed by observations from the field team that noted the hard surface of the snowpack during this time. This means that incoming solar radiation, causing melt and sublimation during the day, is the likely primary driver of measured SWE loss. According to our data, the greatest SWE losses occurred in gullies in VG and on south aspect slopes of the surrounding forested hillslopes. These are also the areas that receive the most direct incoming solar radiation. This finding aligns with work by Musselman et al. (2008), who also observed midwinter SWE loss driven by incoming solar radiation in VCNP.

We hypothesize that the snowpack would become partially isothermal during the day and start to melt and the surface would refreeze at night. The three UAVSAR flights occurred between 9:30-10:30 AM when the snowpack was still mostly frozen, allowing the radar signal to hold coherence even though some LWC was still likely present in the snowpack (Webb et al., 2021a). While the pit data noted minor melting for both the 20 and 26 February pits, it is important to clarify that the snow pits were collected 3 hours after the radar data acquisition. This confirms the findings of Bonnell et al. (2021), suggesting that during the melt season where there is still a freeze-thaw diurnal pattern, the 6:00 AM acquisition timing could hold coherence well enough to track snow that had melted during the day and refrozen over night. For SWE loss to occur with this hypothesis, melted snow needs to exit the snowpack or flow downslope. If melted snow is moving through the entire snowpack, it will not be entirely refrozen based on the meteorological data. It is possible that lateral flow within the snowpack (?Evans et al., 2016) is moving snowmelt downslope between acquisitions.

Both the spatial distribution of SWE change patterns and the magnitude of these patterns make sense, when assuming insolation is the primary mechanism driving SWE change during this time period. These patterns are confirmed by visual comparing the ΔSWE to ΔfSCA (Figure 13). There are noticeable similarities in the areas of greatest loss between the two datasets. The variation in acquisition time period and different parameters being measured do not allow for a direct quantitative comparison. However, when Marshall et al. (2021) compared lidar snow depth change to the UAVSAR phased-based depth retrievals, they found the overall distribution of depth changes and spatial patterns agreed remarkably well. These results add confidence to the findings presented here. Our GPR data provide further justification in our analysis beyond single point comparisons. Future GPR analyses will benefit from validation data collected over larger areas and synchronous timing with remote sensing acquisitions.

The 19-26 February pair is of particular interest because the snowfall event (Figure 11) that occurred on 22 February, in the vicinity of Redondo Peak. This snow accumulation event was detected by the InSAR data, in situ snow depth sensors, and interval boards in the area of the BA snow pit. The lower elevations showed no accumulation in the InSAR retrievals, and this was confirmed by both the HQ met snow depth sensors and snow pit (Figure 8b). These results illustrate the ability to

track both snow ablation and accumulation within the same radar swath, furthering our confidence in the techniques ability to measure ΔSWE in a wide range of conditions.

390   Corresponding research by Webb et al. (2021b) investigated the relationship between dielectric permittivity and LWC for both dry and wet snow conditions in the Jemez Mountains. With ρ_s ranging between 261 to 309 kg m^{-3} and ϵ_s between 1.26 to 1.39, snowpack LWC would range approximately between 3% to 5%. This validates figures presented in Leinss et al. (2015), which state that at L-band (1.26 Ghz), and a ρ_s of 300 kg m^{-3}, the radar signal can penetrate between about 10 m at 1% LWC and 1 m at 10% LWC. The high quality of the phase signal even with relatively high LWC shows promise for

395   the overall performance of NISAR and it's 6 AM and 6 AM sun-synchronous orbit even when snowpacks contain some LWC (Webb et al., 2021b). By processing the 12-26 February pair, we've shown that coherence can be held and quality snow phase information can be obtained at a 14 day temporal baseline, even in the presence of melt. This further supports the robustness of the technique.

4.2   Errors and Uncertainty

400   Our results provide an initial evaluation of the accuracy of the InSAR-derived SWE changes. Our comparison between the InSAR and GPR ΔSWE suggests a conservative maximum bias of ~2 cm for the area near the HQ snow pit. In context with other techniques, airborne lidar has been shown to have uncertainty on the order of 7-8 cm for snow depth (Currier et al., 2019) that when combined with a ρ_s model with additional uncertainty of ~50 kg m^{-3} results in a similar to greater magnitude of SWE uncertainty for the relatively shallow snowpack that develops in the VCNP (Raleigh and Small, 2017). We anticipate the

405   uncertainty to be reduced through future studies discussed further below. Furthermore, this method shows promise for lightly forested areas that were difficult to directly assess in our present study.

The atmospheric correction developed in this study is specific to the UAVSAR data we used. It assumes a homogeneous delay related to the PLV. This delay is mostly likely due to pressure and temperature differences between radar acquisitions, but does not account for smaller spatial scale water vapor variations in the atmospheric delay signal within the radar swath. While

410   we're confident the correction results the method provided for the 12-19 February and 12-26 February pairs, the consistency of near-to-far-range phase ramp in these pairs is unique within the SnowEx UAVSAR dataset, and this method won't be directly applicable to all situations.

We held the ϵ_s values constant for the entire scene. While a single value may be sufficient for the VG meadow, the entire processed scene has more topographic and climatic variation, and therefore ϵ_s and ρ_s variability within the snowpack. We

415   used in situ ϵ_s values for this study that accounted for snowpack LWC, instead of estimating it from density like past studies (Rott et al., 2003; Deeb et al., 2011; Guneriussen et al., 2000). Eppler et al. (2022) found that error in ρ_s estimates only biases total SWE change by <5% for completely dry snow. This uncertainty is likely larger in our analysis due to known LWC in the snowpack. We showed that L-band InSAR can hold coherence with low (~1-5%) levels of snowpack LWC. This adds complexity to the retrievals and should be the topic of future investigations. A variation in LWC between acquisitions will

420   impact radar wave propagation speed and refraction angle in the snowpack, causing a phase shift that resembles a fluctuation in SWE, which could be either a gain or loss. The ambiguity between LWC and SWE variations affecting ϕ_{snow} is resolved by

using in situ data to understand the atmospheric and snowpack dynamics between the flights. For this reason, we limited the geographic scope of this study where field teams evaluated snowpack conditions in the VG meadow, motivated by or goal to confidently validate the ΔSWE retrievals.

425   The phase returns in this study were tethered to a known change point using the in situ snow pit data. This method assumes that there was no variation in SWE or ϵ_s at this point between the three radar acquisitions. For future NISAR data, a time series could be initiated starting with a snow free scene. In such a scenario, any phase delay will be related to the new snow accumulated on the ground. The lack of temporal consistency of the suborbital UAVSAR measurements did not allow for the implementation of this methodology in this work.

430   We created new θ data using a high resolution lidar DEM because of errors within the SRTM DEM provided. NISAR will use the TanDEM-X derived 30 m Copernicus DEM, which does not show the same inaccuracies as SRTM (Rizzoli et al., 2017), and therefore will not be of significant concern. However, all further studies utilizing SnowEx UAVSAR data should inspect the θ raster provided before employing it in the SWE change inversion equation. If errors are found, new θ data should be generated using the Copernicus DEM or other methods (e.g., lidar) to minimize parameter uncertainty.

435   ### 4.3   Future Work

The SnowEx 2020 and 2021 campaigns collected UAVSAR time series data at 14 different research sites across the WUS. Future analysis of this large dataset should focus on quantifying the uncertainties within the SWE retrieval technique. This includes but is not limited to: (1) the impacts of θ, slope, and aspect on the SWE returns; (2) the influence various forest cover metrics; (3) constructing a consistent ΔSWE time series to prepare for NISAR's 12-day temporal repeat; and (4) implementa-
440   tion of spatially distributed ρ_s, ϵ_s, and LWC data into the SWE change equation. This could be derived from snowpack energy balance models (Marks et al., 1999; Liston and Elder, 2006) or through polarimetric radar retrievals (Shi and Dozier, 2000).

Previously, InSAR data has been used to measure geologic processes that vary at slower spatiotemporal scales than mountain SWE, and therefore image pairs could be selectively chosen to have minimal decorrelation and atmospheric effects. However, this is not the case for InSAR-based SWE monitoring, which requires a complete time series of snow accumulation and ablation
445   throughout the winter season, due to rapid decorrelation in snow covered regions.

The ability to confidently identify and correct for a spatially and temporally varying atmospheric signals over mountain range scales is one of the main challenges facing this technique. To address this atmospheric limitation, additional orbital snow specific correction methods must be developed. Future work should leverage past studies utilizing MODIS and other imaging spectrometers (Li et al., 2009), high resolution weather models (Liu et al., 2009), GPS measurements (Li et al., 2006), and
450   combinations of these techniques in tandem (Bekaert et al., 2015). While NISAR data products will include ionospheric and tropospheric correction layers at 80 m spatial resolution, these corrections are automated and may not be temporally consistent enough for snow measurement purposes.

Furthermore, while the ΔSWE results are InSAR-derived, this technique requires a multi-sensor approach for correct implementation. Optical fSCA data are needed to identify snow covered pixels as part of correction for atmospheric delay and
455   to apply the SWE inversion equation over only snow covered pixels. The Landsat 8 image data used in this study represented

two of the very few cloud free days throughout the winter time series over VCNP. To account for the significant issue of cloud cover, future investigations should leverage optical sensor fusion and interpolation methods (Rittger et al., 2021; Dozier et al., 2008) and focus on how to best combine SAR and optical data for SWE change monitoring. Any future SAR-derived SWE product such as the Ku- and X-band approach (Tsang et al., 2022), or the P-band Signals of Opportunity (SoOp) (Yueh et al.,
460 2021) will require optical data to delineate snow covered pixels in midlatitude mountain environments, making this sensor fusion research applicable for radars other than NISAR. Continued work on how to best fuse disparate sensors through cloud computing and machine learning will be key to progressing our knowledge of mountain snowpack monitoring. (Durand et al., 2021).

5   Conclusions

465 This work leveraged high resolution (6 m) UAVSAR interferometric data products to estimate ΔSWE at scales relevant to basin scale water resource management. We developed and applied open-source processing tools to utilize UAVSAR data to detect both positive and negative changes in SWE. We then used in situ snow depth measurements, ΔfSCA, and GPR SWE data to validate the InSAR SWE returns. These results show the robust ability of L-band InSAR to hold coherence and provide quality ΔSWE information even in relatively adverse conditions for radar remote sensing. This research is the first in a series
470 of studies analyzing the SnowEx UAVSAR dataset in preparation for the launch of NISAR in early 2024.

NISAR's low latency (~2 days) cloud-based data products will provide the opportunity to implement this L-band InSAR SWE monitoring technique at continental scales. While there is significant progress needed to better understand uncertainties associated with the retrievals, NISAR's L-band InSAR will have the ability to confidently estimate SWE variations in locations without dense forest cover. Spatiotemporally complete data will require fusion with optical sensors and assimilation in land
475 surface models. We believe that NISAR has the potential to revolutionize the way SWE is measured from spaceborne remote sensing.

Code and data availability.   The code used to perform this analysis and create the figures is publicly available at (https://doi.org/10.5281/zenodo.7199791). The uavsar_pytools package is archived at (https://doi.org/10.5281/zenodo.6578192). UAVSAR data is publicly available at the NASA Jet Propulsion Laboratory UAVSAR data portal (https://uavsar.jpl.nasa.gov/cgi-bin/data.pl, last access: 6 June 2022) and the Alaska Satellite Fa-
480 cility (ASF) Vertex data portal (https://search.asf.alaska.edu/, last access: 6 June 2022). Landsat fSCA data (U.S. Geological Survey and Center, 2018) are publicly available through the United States Geologic Survey (USGS) EarthExplorer data portal (https://earthexplorer.usgs.gov/, last access: 8 March 2022). The Western Regional Climate Center (WRCC) climate station data are publicly available (https://wrcc.dri.edu/vallescaldera/, last access: 8 July 2022). SnowEx20 Time Series Snow Pit Measurements and SnowEx20 Jemez UNM 800 MHz MALA GPR, Version 1 data are publicly available at the NASA National Snow and Ice Data Center Distributed Active Archive Center (NSIDC) (https://nsidc.org/data/snowex,
485 last access: 4 June 2022). Snow depth sensor data is available upon request.

Author contributions. JT, RWW, and HPM conceptualized the overall study. JT and RWW performed the data processing and analysis. JT, RWW, and AWN drafted and edited the manuscript, with FJM and HPM providing helpful comments. AWN, HPM, and RWW provided financial support for the study.

Competing interests. The contact author declares that none of the authors have any competing interests.

490   *Acknowledgements.* Funding for this work was provided by the NASA grant numbers NNX17AL40G (PI: Nolin), 80NSSC18K1405 (Co-I: Webb), and NNX17AL61G (PI: Marshall). Bureau of Reclamation also provided funding with grant number R21AC10459 (Webb). We would like to thank Yunling Lou and the UAVSAR processing team, Dr. Noah Molotch and Leanne Lestak for providing snow depth data, and the SnowEx field teams, especially Adrian Marziliano, who collected in situ observations. The authors would also like to thank Zach Keskinen, Ross Palomaki, Naheem Adebisi for their input and review of the code for this study.

References

A2 Photonic WISe, https://a2photonicsensors.com/wise-sensor-liquid-water-content-snow/, 2021.

Bales, R. C., Molotch, N. P., Painter, T. H., Dettinger, M. D., Rice, R., and Dozier, J.: Mountain Hydrology of the Western United States, Water Resources Research, 42, https://doi.org/10.1029/2005WR004387, 2006.

Balzter, H.: Forest Mapping and Monitoring with Interferometric Synthetic Aperture Radar (InSAR), Progress in Physical Geography: Earth and Environment, 25, 159–177, https://doi.org/10.1177/030913330102500201, 2001.

Bekaert, D., Walters, R., Wright, T., Hooper, A., and Parker, D.: Statistical Comparison of InSAR Tropospheric Correction Techniques, Remote Sensing of Environment, 170, 40–47, https://doi.org/10.1016/j.rse.2015.08.035, 2015.

Bonnell, R., McGrath, D., Williams, K., Webb, R., Fassnacht, S. R., and Marshall, H.-P.: Spatiotemporal Variations in Liquid Water Content in a Seasonal Snowpack: Implications for Radar Remote Sensing, Remote Sensing, 13, 4223, https://doi.org/10.3390/rs13214223, 2021.

Bradford, J. H., Clement, W. P., and Barrash, W.: Estimating Porosity with Ground-Penetrating Radar Reflection Tomography: A Controlled 3-D Experiment at the Boise Hydrogeophysical Research Site, Water Resources Research, 45, https://doi.org/10.1029/2008WR006960, 2009.

Brucker, L., Elder, K., Deems, J., and Newlin, J.: NASA SnowEx 2020 Experiment Plan, p. 100, 2019.

Chen, C. W. and Zebker, H. A.: Two-Dimensional Phase Unwrapping with Use of Statistical Models for Cost Functions in Nonlinear Optimization, Journal of the Optical Society of America A, 18, 338, https://doi.org/10.1364/JOSAA.18.000338, 2001.

Conde, V., Nico, G., Mateus, P., Catalão, J., Kontu, A., and Gritsevich, M.: On The Estimation of Temporal Changes of Snow Water Equivalent by Spaceborne Sar Interferometry: A New Application for the Sentinel-1 Mission, Journal of Hydrology and Hydromechanics, 67, 93–100, https://doi.org/10.2478/johh-2018-0003, 2019.

Currier, W. R., Pflug, J., Mazzotti, G., Jonas, T., Deems, J. S., Bormann, K. J., Painter, T. H., Hiemstra, C. A., Gelvin, A., Uhlmann, Z., Spaete, L., Glenn, N. F., and Lundquist, J. D.: Comparing Aerial Lidar Observations With Terrestrial Lidar and Snow-Probe Transects From NASA's 2017 SnowEx Campaign, Water Resources Research, 55, 6285–6294, https://doi.org/10.1029/2018WR024533, 2019.

Danklmayer, A., Doring, B., Schwerdt, M., and Chandra, M.: Assessment of Atmospheric Propagation Effects in SAR Images, IEEE Transactions on Geoscience and Remote Sensing, 47, 3507–3518, https://doi.org/10.1109/TGRS.2009.2022271, 2009.

Deeb, E. J., Forster, R. R., and Kane, D. L.: Monitoring Snowpack Evolution Using Interferometric Synthetic Aperture Radar on the North Slope of Alaska, USA, International Journal of Remote Sensing, 32, 3985–4003, https://doi.org/10.1080/01431161003801351, 2011.

Deems, J. S., Fassnacht, S. R., and Elder, K. J.: Fractal Distribution of Snow Depth from Lidar Data, Journal of Hydrometeorology, 7, 285–297, https://doi.org/10.1175/JHM487.1, 2006.

Derksen, C., Walker, A., LeDrew, E., and Goodison, B.: Time-Series Analysis of Passive-Microwave-Derived Central North American Snow Water Equivalent Imagery, Annals of Glaciology, 34, 1–7, https://doi.org/10.3189/172756402781817815, 2002.

Dozier, J., Painter, T. H., Rittger, K., and Frew, J. E.: Time–Space Continuity of Daily Maps of Fractional Snow Cover and Albedo from MODIS, Advances in Water Resources, 31, 1515–1526, https://doi.org/10.1016/j.advwatres.2008.08.011, 2008.

Durand, M., Barros, A., Dozier, J., Adler, R., Cooley, S., Entekhabi, D., Forman, B. A., Konings, A. G., Kustas, W. P., Lundquist, J. D., Pavelsky, T. M., Rodell, M., and Steele-Dunne, S.: Achieving Breakthroughs in Global Hydrologic Science by Unlocking the Power of Multisensor, Multidisciplinary Earth Observations, AGU Advances, 2, e2021AV000 455, https://doi.org/10.1029/2021AV000455, 2021.

Eppler, J., Rabus, B., and Morse, P.: Snow Water Equivalent Change Mapping from Slope-Correlated Synthetic Aperture Radar Interferometry (InSAR) Phase Variations, The Cryosphere, p. 25, 2022.

Evans, S. L., Flores, A. N., Heilig, A., Kohn, M. J., Marshall, H.-P., and McNamara, J. P.: Isotopic Evidence for Lateral Flow and Diffusive Transport, but Not Sublimation, in a Sloped Seasonal Snowpack, Idaho, USA, Geophysical Research Letters, 43, 3298–3306, https://doi.org/10.1002/2015GL067605, 2016.

535 Farr, T. G., Rosen, P. A., Caro, E., Crippen, R., Duren, R., Hensley, S., Kobrick, M., Paller, M., Rodriguez, E., Roth, L., Seal, D., Shaffer, S., Shimada, J., Umland, J., Werner, M., Oskin, M., Burbank, D., and Alsdorf, D.: The Shuttle Radar Topography Mission, Reviews of Geophysics, 45, https://doi.org/10.1029/2005RG000183, 2007.

Ferretti, A., Prati, C., and Rocca, F.: Permanent Scatterers in SAR Interferometry, IEEE Transactions on Geoscience and Remote Sensing, 39, 8–20, https://doi.org/10.1109/36.898661, 2001.

540 Foster, J. L., Sun, C., Walker, J. P., Kelly, R., Chang, A., Dong, J., and Powell, H.: Quantifying the Uncertainty in Passive Microwave Snow Water Equivalent Observations, Remote Sensing of Environment, 94, 187–203, https://doi.org/10.1016/j.rse.2004.09.012, 2005.

Goldstein, R. M. and Zebker, H. A.: Interferometric Radar Measurement of Ocean Surface Currents, Nature, 328, 707–709, https://doi.org/10.1038/328707a0, 1987.

Goldstein, R. M., Zebker, H. A., and Werner, C. L.: Satellite Radar Interferometry: Two-dimensional Phase Unwrapping, Radio Science, 23, 545 713–720, https://doi.org/10.1029/RS023i004p00713, 1988.

Gubler, H. and Hiller, M.: The Use of Microwave FMCW Radar in Snow and Avalanche Research, Cold Regions Science and Technology, 9, 109–119, https://doi.org/10.1016/0165-232X(84)90003-X, 1984.

Guneriussen, T., Hogda, K., Johnsen, H., and Lauknes, I.: InSAR for Estimation of Changes in Snow Water Equivalent of Dry Snow, in: IGARSS 2000. IEEE 2000 International Geoscience and Remote Sensing Symposium. Taking the Pulse of the Planet: The Role of 550 Remote Sensing in Managing the Environment. Proceedings (Cat. No.00CH37120), vol. 2, pp. 463–466, IEEE, Honolulu, HI, USA, https://doi.org/10.1109/IGARSS.2000.861597, 2000.

Harpold, A., Molotch, N. P., Musselman, K. N., Bales, R. C., Kirchner, P. B., Litvak, M., and Brooks, P. D.: Soil Moisture Response to Snowmelt Timing in Mixed-Conifer Subalpine Forests, Hydrological Processes, 29, 2782–2798, https://doi.org/10.1002/hyp.10400, 2015.

Heilig, A., Mitterer, C., Schmid, L., Wever, N., Schweizer, J., Marshall, H.-P., and Eisen, O.: Seasonal and Diurnal Cycles 555 of Liquid Water in Snow—Measurements and Modeling, Journal of Geophysical Research: Earth Surface, 120, 2139–2154, https://doi.org/10.1002/2015JF003593, 2015.

Hensley, S., Wheeler, K., Sadowy, G., Jones, C., Shaffer, S., Zebker, H., Miller, T., Heavey, B., Chuang, E., Chao, R., Vines, K., Nishimoto, K., Prater, J., Carrico, B., Chamberlain, N., Shimada, J., Simard, M., Chapman, B., Muellerschoen, R., Le, C., Michel, T., Hamilton, G., Robison, D., Neumann, G., Meyer, R., Smith, P., Granger, J., Rosen, P., Flower, D., and Smith, R.: The UAVSAR Instrument: Description 560 and First Results, in: 2008 IEEE Radar Conference, pp. 1–6, IEEE, Rome, Italy, https://doi.org/10.1109/RADAR.2008.4720722, 2008.

Holbrook, W. S., Miller, S. N., and Provart, M. A.: Estimating Snow Water Equivalent over Long Mountain Transects Using Snowmobile-Mounted Ground-Penetrating Radar, GEOPHYSICS, 81, WA183–WA193, https://doi.org/10.1190/geo2015-0121.1, 2016.

Keskinen, Z. and Tarricone, J.: Uavsar_pytools, Zenodo, https://doi.org/10.5281/zenodo.6789624, 2022.

King, J., Derksen, C., Toose, P., Langlois, A., Larsen, C., Lemmetyinen, J., Marsh, P., Montpetit, B., Roy, A., Rutter, N., and Sturm, M.: The 565 Influence of Snow Microstructure on Dual-Frequency Radar Measurements in a Tundra Environment, Remote Sensing of Environment, 215, 242–254, https://doi.org/10.1016/j.rse.2018.05.028, 2018.

Leinss, S., Wiesmann, A., Lemmetyinen, J., and Hajnsek, I.: Snow Water Equivalent of Dry Snow Measured by Differential Interferometry, IEEE Journal of Selected Topics in Applied Earth Observations and Remote Sensing, 8, 3773–3790, https://doi.org/10.1109/JSTARS.2015.2432031, 2015.

570 Lettenmaier, D. P., Alsdorf, D., Dozier, J., Huffman, G. J., Pan, M., and Wood, E. F.: Inroads of Remote Sensing into Hydrologic Science during the WRR Era: REMOTE SENSING, Water Resources Research, 51, 7309–7342, https://doi.org/10.1002/2015WR017616, 2015.

Lewis, G., Osterberg, E., Hawley, R., Whitmore, B., Marshall, H. P., and Box, J.: Regional Greenland Accumulation Variability from Operation IceBridge Airborne Accumulation Radar, The Cryosphere, 11, 773–788, https://doi.org/10.5194/tc-11-773-2017, 2017.

Li, D., Wrzesien, M. L., Durand, M., Adam, J., and Lettenmaier, D. P.: How Much Runoff Originates as Snow in the Western United States,
575 and How Will That Change in the Future?: Western U.S. Snowmelt-Derived Runoff, Geophysical Research Letters, 44, 6163–6172, https://doi.org/10.1002/2017GL073551, 2017a.

Li, H., Wang, Z., He, G., and Man, W.: Estimating Snow Depth and Snow Water Equivalence Using Repeat-Pass Interferometric SAR in the Northern Piedmont Region of the Tianshan Mountains, Journal of Sensors, 2017, 1–17, https://doi.org/10.1155/2017/8739598, 2017b.

Li, Z., Fielding, E. J., Cross, P., and Muller, J.-P.: Interferometric Synthetic Aperture Radar Atmospheric Correction: GPS Topography-
580 Dependent Turbulence Model: INTEGRATION OF GPS AND INSAR, Journal of Geophysical Research: Solid Earth, 111, n/a–n/a, https://doi.org/10.1029/2005JB003711, 2006.

Li, Z., Fielding, E. J., Cross, P., and Preusker, R.: Advanced InSAR Atmospheric Correction: MERIS/MODIS Combination and Stacked Water Vapour Models, International Journal of Remote Sensing, 30, 3343–3363, https://doi.org/10.1080/01431160802562172, 2009.

Lievens, H., Demuzere, M., Marshall, H.-P., Reichle, R. H., Brucker, L., Brangers, I., de Rosnay, P., Dumont, M., Girotto, M., Immerzeel,
585 W. W., Jonas, T., Kim, E. J., Koch, I., Marty, C., Saloranta, T., Schöber, J., and De Lannoy, G. J. M.: Snow Depth Variability in the Northern Hemisphere Mountains Observed from Space, Nature Communications, 10, 4629, https://doi.org/10.1038/s41467-019-12566-y, 2019.

Lievens, H., Brangers, I., Marshall, H.-P., Jonas, T., Olefs, M., and De Lannoy, G.: Sentinel-1 Snow Depth Retrieval at Sub-Kilometer Resolution over the European Alps, The Cryosphere, 16, 159–177, https://doi.org/10.5194/tc-16-159-2022, 2022.

590 Liston, G. E. and Elder, K.: A Distributed Snow-Evolution Modeling System (SnowModel), Journal of Hydrometeorology, 7, 1259–1276, https://doi.org/10.1175/JHM548.1, 2006.

Liu, S., Hanssen, R., and Mika, Á.: On the Value of High-Resolution Weather Models for Atmospheric Mitigation in SAR Interferometry, in: 2009 IEEE International Geoscience and Remote Sensing Symposium, vol. 2, pp. II–749–II–752, https://doi.org/10.1109/IGARSS.2009.5418199, 2009.

595 Lund, J., Forster, R. R., Rupper, S. B., Deeb, E. J., Marshall, H. P., Hashmi, M. Z., and Burgess, E.: Mapping Snowmelt Progression in the Upper Indus Basin With Synthetic Aperture Radar, Frontiers in Earth Science, 7, 318, https://doi.org/10.3389/feart.2019.00318, 2020.

Marks, D., Domingo, J., Susong, D., Link, T., and Garen, D.: A Spatially Distributed Energy Balance Snowmelt Model for Application in Mountain Basins, Hydrological Processes, 13, 1935–1959, https://doi.org/10.1002/(SICI)1099-1085(199909)13:12/13<1935::AID-HYP868>3.0.CO;2-C, 1999.

600 Marshall, H., Deeb, E., Forster, R., Vuyovich, C., Elder, K., Hiemstra, C., and Lund, J.: L-Band InSAR Depth Retrieval During the NASA SnowEx 2020 Campaign: Grand Mesa, Colorado, in: 2021 IEEE International Geoscience and Remote Sensing Symposium IGARSS, pp. 625–627, https://doi.org/10.1109/IGARSS47720.2021.9553852, 2021.

Marshall, H.-P. and Koh, G.: FMCW Radars for Snow Research, Cold Regions Science and Technology, 52, 118–131, https://doi.org/10.1016/j.coldregions.2007.04.008, 2008.

605 Marshall, H.-P., Koh, G., and Forster, R. R.: Estimating Alpine Snowpack Properties Using FMCW Radar, Annals of Glaciology, 40, 157–162, https://doi.org/10.3189/172756405781813500, 2005.

Marshall, H.-P., Mason, M., McCormick, M., Craaybeek, D., Elder, K., Vuyovich, C., and Time Series Site Leads and Field Teams: SnowEx20 Time Series Snow Pit Measurements [Jemez River]. [Date Accessed: 14 October 2022]., https://doi.org/10.5067/POT9E0FFUUD1, 2022.

McGrath, D., Sass, L., O'Neel, S., McNeil, C., Candela, S. G., Baker, E. H., and Marshall, H.-P.: Interannual Snow Accumulation Variability on Glaciers Derived from Repeat, Spatially Extensive Ground-Penetrating Radar Surveys, The Cryosphere, 12, 3617–3633, https://doi.org/10.5194/tc-12-3617-2018, 2018.

Meyer, F. J.: Performance Requirements for Ionospheric Correction of Low-Frequency SAR Data, IEEE Transactions on Geoscience and Remote Sensing, 49, 3694–3702, https://doi.org/10.1109/TGRS.2011.2146786, 2011.

Michaelides, R. J., Chen, R. H., Zhao, Y., Schaefer, K., Parsekian, A. D., Sullivan, T., Moghaddam, M., Zebker, H. A., Liu, L., Xu, X., and Chen, J.: Permafrost Dynamics Observatory—Part I: Postprocessing and Calibration Methods of UAVSAR L-Band InSAR Data for Seasonal Subsidence Estimation, Earth and Space Science, 8, https://doi.org/10.1029/2020EA001630, 2021.

Milly, P. C. D., Betancourt, J., Falkenmark, M., Hirsch, R. M., Kundzewicz, Z. W., Lettenmaier, D. P., and Stouffer, R. J.: Stationarity Is Dead: Whither Water Management?, Science, 319, 573–574, https://doi.org/10.1126/science.1151915, 2008.

Molotch, N. P., Brooks, P. D., Burns, S. P., Litvak, M., Monson, R. K., McConnell, J. R., and Musselman, K.: Ecohydrological Controls on Snowmelt Partitioning in Mixed-Conifer Sub-Alpine Forests, Ecohydrology, 2, 129–142, https://doi.org/10.1002/eco.48, 2009.

Mote, P. W., Li, S., Lettenmaier, D. P., Xiao, M., and Engel, R.: Dramatic Declines in Snowpack in the Western US, npj Climate and Atmospheric Science, 1, 2, https://doi.org/10.1038/s41612-018-0012-1, 2018.

Mouginot, J.: Mapping of Ice Motion in Antarctica Using Synthetic-Aperture Radar Data, p. 15, 2012.

Musselman, K. N., Molotch, N. P., and Brooks, P. D.: Effects of Vegetation on Snow Accumulation and Ablation in a Mid-Latitude Sub-Alpine Forest, Hydrological Processes, 22, 2767–2776, https://doi.org/10.1002/hyp.7050, 2008.

Nagler, T. and Rott, H.: Retrieval of Wet Snow by Means of Multitemporal SAR Data, IEEE Transactions on Geoscience and Remote Sensing, 38, 754–765, https://doi.org/10.1109/36.842004, 2000.

Nagler, T., Rott, H., Ripper, E., Bippus, G., and Hetzenecker, M.: Advancements for Snowmelt Monitoring by Means of Sentinel-1 SAR, Remote Sensing, 8, 348, https://doi.org/10.3390/rs8040348, 2016.

Nagler, T., Rott, H., Scheiblauer, S., Libert, L., Mölg, N., Horn, R., Fischer, J., Keller, M., Moreira, A., and Kubanek, J.: Airborne Experiment on Insar Snow Mass Retrieval in Alpine Environment, in: IGARSS 2022 - 2022 IEEE International Geoscience and Remote Sensing Symposium, pp. 4549–4552, https://doi.org/10.1109/IGARSS46834.2022.9883809, 2022.

Nolin, A., Dozier, J., and Mertes, L.: Mapping Alpine Snow Using a Spectral Mixture Modeling Technique, Annals of Glaciology, 17, 121–124, https://doi.org/doi:10.3189/S0260305500012702, 1993.

OpenTopography: Jemez River Basin Snow-off LiDAR Survey, https://opentopography.org/meta/OT.062012.26913.1, 2012.

Painter, T. H., Rittger, K., McKenzie, C., Slaughter, P., Davis, R. E., and Dozier, J.: Retrieval of Subpixel Snow Covered Area, Grain Size, and Albedo from MODIS, Remote Sensing of Environment, 113, 868–879, https://doi.org/10.1016/j.rse.2009.01.001, 2009.

Painter, T. H., Berisford, D. F., Boardman, J. W., Bormann, K. J., Deems, J. S., Gehrke, F., Hedrick, A., Joyce, M., Laidlaw, R., Marks, D., Mattmann, C., McGurk, B., Ramirez, P., Richardson, M., Skiles, S. M., Seidel, F. C., and Winstral, A.: The Airborne Snow Observatory: Fusion of Scanning Lidar, Imaging Spectrometer, and Physically-Based Modeling for Mapping Snow Water Equivalent and Snow Albedo, Remote Sensing of Environment, 184, 139–152, https://doi.org/10.1016/j.rse.2016.06.018, 2016.

Raleigh, M. S. and Small, E. E.: Snowpack Density Modeling Is the Primary Source of Uncertainty When Mapping Basin-Wide SWE with Lidar: Uncertainties in SWE Mapping With Lidar, Geophysical Research Letters, 44, 3700–3709, https://doi.org/10.1002/2016GL071999, 2017.

645 Rango, A., Chang, A. T. C., and Foster, J. L.: The Utilization of Spaceborne Microwave Radiometers for Monitoring Snowpack Properties, Hydrology Research, 10, 25–40, https://doi.org/10.2166/nh.1979.0003, 1979.

Rittger, K., Krock, M., Kleiber, W., Bair, E. H., Brodzik, M. J., Stephenson, T. R., Rajagopalan, B., Bormann, K. J., and Painter, T. H.: Multi-Sensor Fusion Using Random Forests for Daily Fractional Snow Cover at 30 m, Remote Sensing of Environment, 264, 112 608, https://doi.org/10.1016/j.rse.2021.112608, 2021.

650 Rizzoli, P., Martone, M., Gonzalez, C., Wecklich, C., Borla Tridon, D., Bräutigam, B., Bachmann, M., Schulze, D., Fritz, T., Huber, M., Wessel, B., Krieger, G., Zink, M., and Moreira, A.: Generation and Performance Assessment of the Global TanDEM-X Digital Elevation Model, ISPRS Journal of Photogrammetry and Remote Sensing, 132, 119–139, https://doi.org/10.1016/j.isprsjprs.2017.08.008, 2017.

Rosen, P., Hensley, S., Joughin, I., Li, F., Madsen, S., Rodriguez, E., and Goldstein, R.: Synthetic Aperture Radar Interferometry, Proceedings of the IEEE, 88, 333–382, https://doi.org/10.1109/5.838084, 2000.

655 Rosen, P., Hensley, S., Wheeler, K., Sadowy, G., Miller, T., Shaffer, S., Muellerschoen, R., Jones, C., Zebker, H., and Madsen, S.: UAVSAR: A New NASA Airborne SAR System for Science and Technology Research, in: 2006 IEEE Conference on Radar, pp. 22–29, IEEE, Syracuse, NY, USA, https://doi.org/10.1109/RADAR.2006.1631770, 2006.

Rosen, P., Hensley, S., Shaffer, S., Edelstein, W., Kim, Y., Kumar, R., Misra, T., Bhan, R., and Sagi, R.: The NASA-ISRO SAR (NISAR) Mission Dual-Band Radar Instrument Preliminary Design, in: 2017 IEEE International Geoscience and Remote Sensing Symposium 660 (IGARSS), pp. 3832–3835, https://doi.org/10.1109/IGARSS.2017.8127836, 2017.

Rott, H., Nagler, T., and Scheiber, R.: Snow Mass Retrieval by Means of SAR Interferometry, in: FRINGE '03 Workshop: Advances in SAR Interferometry from ERS and ENVISAT Missions, pp. pp. 1–6, Noordwijk: European Space Agency (ESA) Publications Division, Frascati, Italy, 2003.

Rott, H., Yueh, S. H., Cline, D. W., Duguay, C., Essery, R., Haas, C., Hélière, F., Kern, M., Macelloni, G., Malnes, E., Nagler, T., Pulliainen, J., 665 Rebhan, H., and Thompson, A.: Cold Regions Hydrology High-Resolution Observatory for Snow and Cold Land Processes, Proceedings of the IEEE, 98, 752–765, https://doi.org/10.1109/JPROC.2009.2038947, 2010.

Rutter, N., Sandells, M. J., Derksen, C., King, J., Toose, P., Wake, L., Watts, T., Essery, R., Roy, A., Royer, A., Marsh, P., Larsen, C., and Sturm, M.: Effect of Snow Microstructure Variability on Ku-band Radar Snow Water Equivalent Retrievals, The Cryosphere, 13, 3045–3059, https://doi.org/10.5194/tc-13-3045-2019, 2019.

670 Sandmeier, D. K. J. and Straße, Z.: REFLEXW, 2022.

Selkowitz, D. J., Painter, T. H., Rittger, K., Schmidt, G., and Forster, R.: The USGS Landsat Snow Covered Area Products: Methods and Preliminary Validaiton, 2017.

Shi, J. and Dozier, J.: Estimation of Snow Water Equivalence Using SIR-C/X-SAR. II. Inferring Snow Depth and Particle Size, IEEE Transactions on Geoscience and Remote Sensing, 38, 2475–2488, https://doi.org/10.1109/36.885196, 2000.

675 Siirila-Woodburn, E. R., Rhoades, A. M., Hatchett, B. J., Huning, L. S., Szinai, J., Tague, C., Nico, P. S., Feldman, D. R., Jones, A. D., Collins, W. D., and Kaatz, L.: A Low-to-No Snow Future and Its Impacts on Water Resources in the Western United States, Nature Reviews Earth & Environment, https://doi.org/10.1038/s43017-021-00219-y, 2021.

Stewart, I. T., Cayan, D. R., and Dettinger, M. D.: Changes in Snowmelt Runoff Timing in Western North America under a 'Business as Usual' Climate Change Scenario, Climatic Change, 62, 217–232, https://doi.org/10.1023/B:CLIM.0000013702.22656.e8, 2004.

680 Trujillo, E., Ramírez, J. A., and Elder, K. J.: Topographic, Meteorologic, and Canopy Controls on the Scaling Characteristics of the Spatial Distribution of Snow Depth Fields: SPATIAL SCALING OF SNOW DEPTH, Water Resources Research, 43, https://doi.org/10.1029/2006WR005317, 2007.

Tsang, L., Durand, M., Derksen, C., Barros, A. P., Kang, D.-H., Lievens, H., Marshall, H.-P., Zhu, J., Johnson, J., King, J., Lemmetyinen, J., Sandells, M., Rutter, N., Siqueira, P., Nolin, A., Osmanoglu, B., Vuyovich, C., Kim, E., Taylor, D., Merkouriadi, I., Brucker, L., Navari, M., Dumont, M., Kelly, R., Kim, R. S., Liao, T.-H., Borah, F., and Xu, X.: Review Article: Global Monitoring of Snow Water Equivalent Using High-Frequency Radar Remote Sensing, The Cryosphere, p. 43, 2022.

Ulaby, F. T., Stiles, W. H., and Abdelrazik, M.: Snowcover Influence on Backscattering from Terrain, IEEE Transactions on Geoscience and Remote Sensing, GE-22, 126–133, https://doi.org/10.1109/TGRS.1984.350604, 1984.

U.S. Geological Survey, E. R. O. and Center, S.: Collection-1 Landsat Level-3 Fractional Snow Covered Area (FSCA) Science Product, https://doi.org/10.5066/F7XK8DS5, 2018.

Vuyovich, C. M., Jacobs, J. M., and Daly, S. F.: Comparison of Passive Microwave and Modeled Estimates of Total Watershed SWE in the Continental United States, Water Resources Research, 50, 9088–9102, https://doi.org/10.1002/2013WR014734, 2014.

Webb, R.: SnowEx20 Jemez UNM 800 MHz MALA GPR, Version 1, https://doi.org/10.5067/H38Q5FTBPZ8K, 2020.

Webb, R. W.: Using Ground Penetrating Radar to Assess the Variability of Snow Water Equivalent and Melt in a Mixed Canopy Forest, Northern Colorado, Frontiers of Earth Science, 11, 482–495, https://doi.org/10.1007/s11707-017-0645-0, 2017.

Webb, R. W., Jennings, K. S., Fend, M., and Molotch, N. P.: Combining Ground-Penetrating Radar With Terrestrial LiDAR Scanning to Estimate the Spatial Distribution of Liquid Water Content in Seasonal Snowpacks, Water Resources Research, 54, https://doi.org/10.1029/2018WR022680, 2018.

Webb, R. W., Jennings, K., Finsterle, S., and Fassnacht, S. R.: Two-Dimensional Liquid Water Flow through Snow at the Plot Scale in Continental Snowpacks: Simulations and Field Data Comparisons, The Cryosphere, 15, 1423–1434, https://doi.org/10.5194/tc-15-1423-2021, 2021a.

Webb, R. W., Marziliano, A., McGrath, D., Bonnell, R., Meehan, T. G., Vuyovich, C., and Marshall, H.-P.: In Situ Determination of Dry and Wet Snow Permittivity: Improving Equations for Low Frequency Radar Applications, Remote Sensing, 13, 4617, https://doi.org/10.3390/rs13224617, 2021b.

Yu, C., Li, Z., and Penna, N. T.: Interferometric Synthetic Aperture Radar Atmospheric Correction Using a GPS-based Iterative Tropospheric Decomposition Model, Remote Sensing of Environment, 204, 109–121, https://doi.org/10.1016/j.rse.2017.10.038, 2018.

Yueh, S. H., Dinardo, S. J., Akgiray, A., West, R., Cline, D. W., and Elder, K.: Airborne Ku-Band Polarimetric Radar Remote Sensing of Terrestrial Snow Cover, IEEE Transactions on Geoscience and Remote Sensing, 47, 3347–3364, https://doi.org/10.1109/TGRS.2009.2022945, 2009.

Yueh, S. H., Shah, R., Xu, X., Stiles, B., and Bosch-Lluis, X.: A Satellite Synthetic Aperture Radar Concept Using P-Band Signals of Opportunity, IEEE Journal of Selected Topics in Applied Earth Observations and Remote Sensing, 14, 2796–2816, https://doi.org/10.1109/JSTARS.2021.3059242, 2021.

Zebker, H. A. and Goldstein, R. M.: Topographic Mapping from Interferometric Synthetic Aperture Radar Observations, Journal of Geophysical Research: Solid Earth, 91, 4993–4999, https://doi.org/10.1029/JB091iB05p04993, 1986.

Zebker, H. A., Rosen, P. A., and Hensley, S.: Atmospheric Effects in Interferometric Synthetic Aperture Radar Surface Deformation and Topographic Maps, Journal of Geophysical Research: Solid Earth, 102, 7547–7563, https://doi.org/10.1029/96JB03804, 1997.

Zhu, J., Tan, S., Tsang, L., Kang, D.-H., and Kim, E.: Snow Water Equivalent Retrieval Using Active and Passive Microwave Observations, Water Resources Research, 57, e2020WR027 563, https://doi.org/10.1029/2020WR027563, 2021.
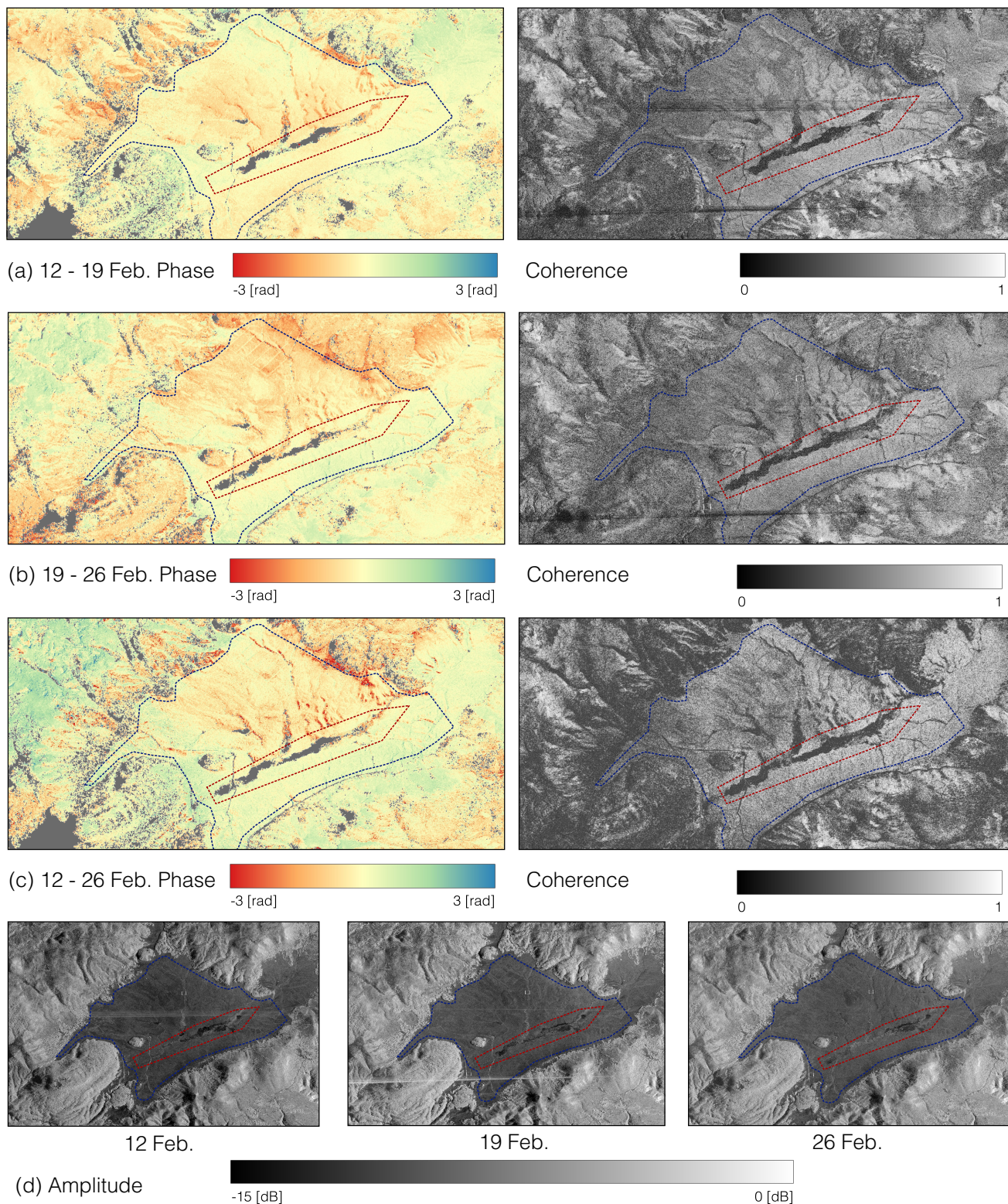
Figure 7. The atmospherically corrected unwrapped phase and coherence data for the (a) 12-19 February (b) 19-26 February (c) 12-26 February InSAR pairs, and (d) the amplitude data for the three UAVSAR flights. The grey area in the phase data are pixels lost in in the unwrapping processes. The VG meadow and Jemez River main channel are outlined by blue and red dotted lines respectively.
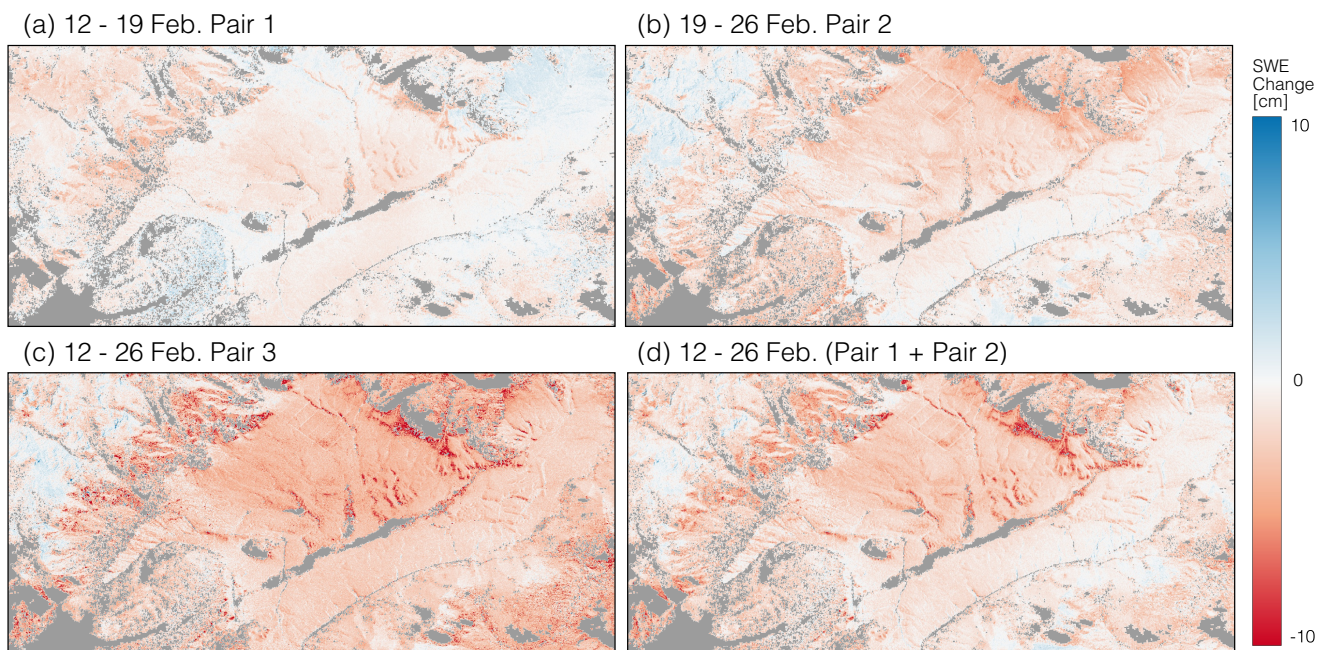
Figure 8. InSAR-derived ΔSWE results for (a) 12-19 February (b) 19-26 February (c) 12-26 February (d) and the cumulative change between 12-26 February generated by adding the data from (a) and (b) together.
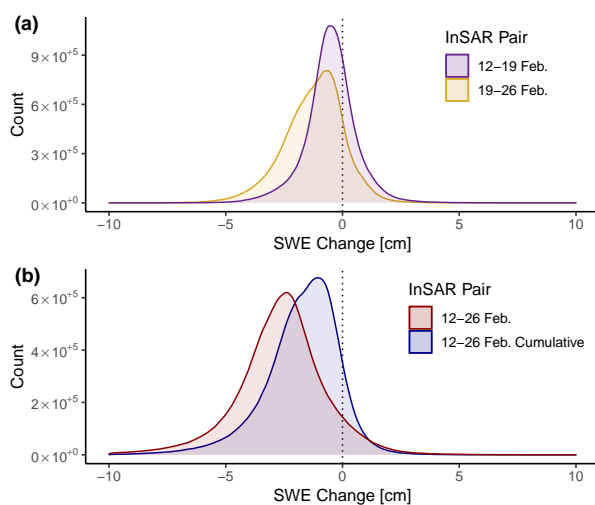
Figure 9. Histograms displaying the distribution of ΔSWE values for (a) 12-19 February and 19-26 February, and (b) 12-26 February and the cumulative change between 12-26 February.
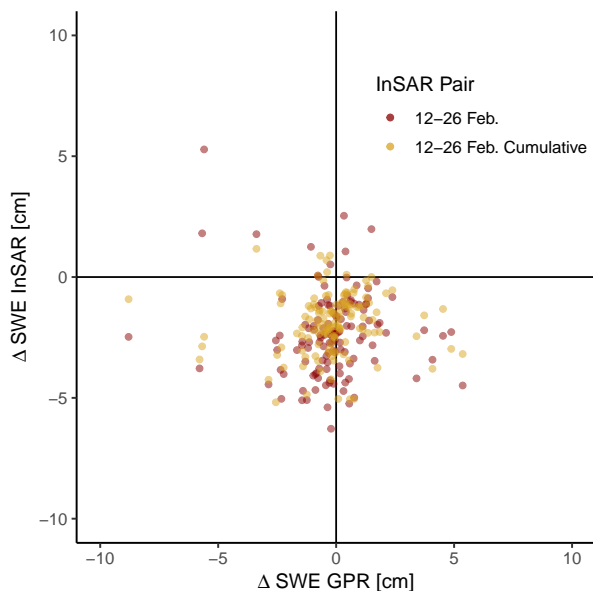
Figure 10. Scatter plot comparing InSAR and GPR derived ΔSWE for the 12-26 February and 12-26 cumulative pairs.
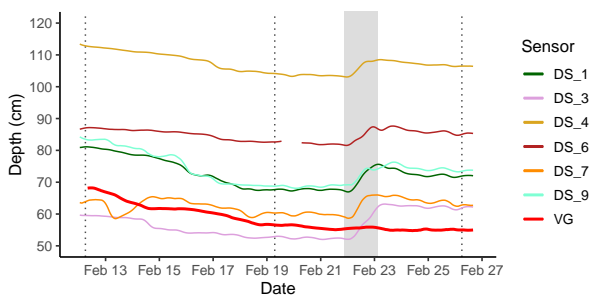
Figure 11. A snow depth time series for six CZO sensors (beginning with DS) on Redondo peak and the HQ met sensor (red) at a lower elevation in VG. All six of the higher elevation CZO sensors show precipitation event starting on 22 February (grey shading), while the HQ sensor does not.
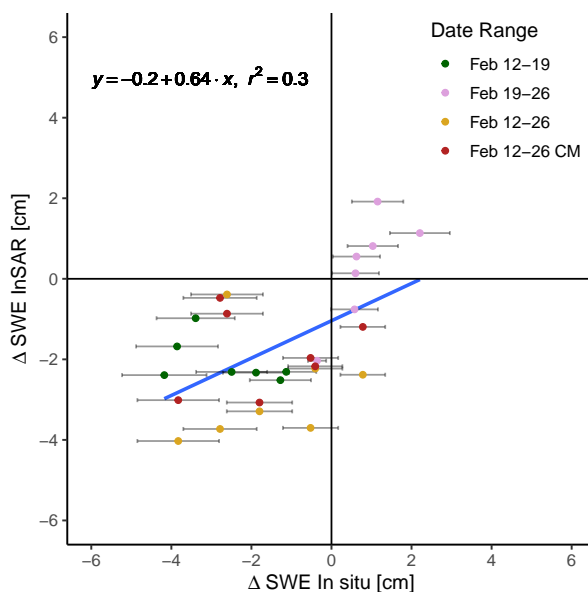
Figure 12. Comparing in situ SWE changes from the six CZO and the HQ met snow depth sensors to InSAR-derived SWE changes for four InSAR pairs. Snow depths are converted to SWE by multiplying by ρ_s from the BA snow pit. The in situ SWE error bars represent a 10% uncertainty from the snow pit density measurements and 2 cm uncertainty from the ultrasonic snow depth sensors.
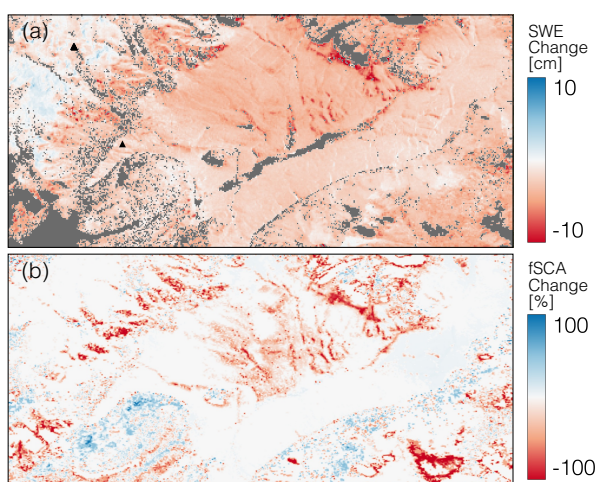
Figure 13. (a) The cumulative InSAR-derived ΔSWE between 12-26 February resampled up to the Landsat resolution of 30 m, and (b) the change in Landsat fSCA between 18 February and 5 March.
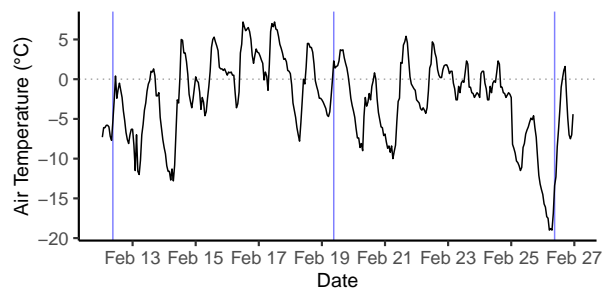
Figure 14. Mean hourly temperature over the study period at HQ meteorologic station in VG during the study period (12-26 February). Temperatures consistently dropped below freezing at night and rose above 0°C during the most days. Blue vertical lines represent the times of the three UAVSAR acquisitions.